REVIEW

Chemical Aspects of Halide Perovskite Nanocrystals

Mrinmoy Roy[1,2] · Milan Sykora[2] · M. Aslam[1]

Abstract

Halide perovskite nanocrystals (HPNCs) are currently among the most intensely investigated group of materials. Structurally related to the bulk halide perovskites (HPs), HPNCs are nanostructures with distinct chemical, optical, and electronic properties and significant practical potential. One of the keys to the effective exploitation of the HPNCs in advanced technologies is the development of controllable, reproducible, and scalable methods for preparation of materials with desired compositions, phases, and shapes and low defect content. Another important condition is a quantitative understanding of factors affecting the chemical stability and the optical and electronic properties of HPNCs. Here we review important recent developments in these areas. Following a brief historical prospective, we provide an overview of known chemical methods for preparation of HPNCs and approaches used to control their composition, phase, size, and shape. We then review studies of the relationship between the chemical composition and optical properties of HPNCs, degradation mechanisms, and effects of charge injection. Finally, we provide a short summary and an outlook. The aim of this review is not to provide a comprehensive summary of all relevant literature but rather a selection of highlights, which, in the subjective view of the authors, provide the most significant recent observations and relevant analyses.

✉ M. Aslam
  m.aslam@iitb.ac.in

1 Department of Physics, Indian Institute of Technology Bombay, Mumbai 400076, India

2 Laboratory for Advanced Materials, Faculty of Natural Sciences, Comenius University, Bratislava 84104, Slovakia

1 Introduction

The first synthetic halide perovskites (HPs) were reported in 1893, when H.L. Wells described preparation of inorganic halide perovskites $CsPbX_3$, $CsPb_2X_5$, and Cs_4PbX_6, (where X is Cl^- and Br^-) [1]. In the 1950s, C.K. Møller not only identified/confirmed the perovskite structure of these cesium lead halides but also observed photoconductivity in these materials. In the 1990s, D.B. Mitzi and coworkers investigated and described magnetic, electronic, optical, and electroluminescent properties of a variety of inorganic and organic–inorganic halide perovskite materials [2–4]. In 2006–2009, in search of more efficient light absorbers, T. Miyasaka and coworkers were the first to use hybrid HP $MAPbX_3$ (MA is $CH_3NH_3^+$ and X is Br^- and I^-) as a light-absorbing layer in a dye-sensitized solar cell and demonstrated first perovskite solar cells with ~3.81% ($MAPbI_3$) and ~3.13% ($MAPbBr_3$) Power conversion efficiencies (PCEs) [5]. Shortly after, teams led by T.N. Murakami, T. Miyasaka, H. Snaith, N.G. Park, and M. Grätzel reported first solid-state perovskite solar cells employing $MAPbI_{3-x}Cl_x$ mixed halide perovskite and $MAPbI_3$ with the PCEs between 8% and 10% [6, 7]. These initial advances stimulated vigorous effort in the development of HP solar cells with various architectures and within a span of few years, at the improvement rate unprecedented for photovoltaic technologies, perovskite solar cells have reached PCEs of 26.1% [8–12]. The tandem solar cells combining the HPs with Si have recently reached a record PCE of 32.5% [13]. Despite of the great promise, the commercial exploitation of HP solar cells faces challenges associated with the limited thermal and chemical stability of HPs and toxicity associated with the presence of lead. Intensive research is currently underway to explore solutions for overcoming these challenges and advancing the industrialization of photovoltaics [14, 15].

Shortly after the initial reports describing the preparation and properties of HP solar cells, several studies [16–18] showed that unusual excitonic and charge transport properties of HPs could be exploited not only for applications requiring light-induced charge separation and production of current but also for applications where the processes are reversed, i.e., where injected charges recombine radiatively together under an applied external potential. High color purity and low intrinsic rate of nonradiative recombination make HPs very appealing candidates for development of light-emitting diodes (LEDs) and lasers [19]. However, some early studies also revealed that bulk HPs, formed as solid films, have relatively low photoluminescence quantum yields (PLQY), primarily due to the defects forming during the heating and solvent evaporation step of the spin-cast process [20]. The defects at the grain boundaries of the HP crystallites were shown to act as fast nonradiative recombination centers, contributing to observation of a weak photoluminescence (PL) [21]. An important advance in this area was a report by Droseros et al. [22] who showed that PLQY of HPs could be significantly improved simply by reducing the size of the grains from the micrometer- to millimeter-size range crystallites, typical for HP thin films, to the nanometer-size crystals. The improved PLQY in nanocrystals (NCs) was shown to be due to the improved passivation of surface traps and resulting increase in the fraction of excited states decaying radiatively.

The observation of enhanced PL in nanocrystalline HPs and the first reports on solution-based synthesis of HPNCs in 2014 (Fig. 1) [23], have stimulated growing interest in this class of materials. The transition into nanoregime not only helps to increase PLQY but also provides an access to tunability of the electronic structure via the quantum confinement effects. Within a few years, syntheses of high-quality HPNCs with various chemical compositions, sizes, and shapes were reported. The experimental results show that in HPNCs halogen type, structure, size, and phase can be controlled not only during the synthesis but also during the postsynthesis processing (i.e., ion exchange, amine treatment, external photon radiation, etc.). The increased quantum confinement resulting from reduction in size of the crystals at the nanoscale leads to enhanced radiative recombination, which is beneficial for the light-emitting applications. Reduction in the size, however, also leads to an increase in the surface to volume ratio and potentially higher defect concentration. The point defects can also be introduced by doping of HPNCs. Another important challenge is the chemical and phase stability of HPNCs upon exposure to various environmental factors as well as under conditions of applied potential. Understanding of the interplay of these factors is essential for effective exploitation of the benefits of the HPNCs in optoelectronic applications. In this review, we provide a summary of recent literature that, in our view, provides the most relevant analyses and answers to these important challenges and questions.

2 Structure of Halide Perovskites

In bulk HPs, with the general chemical formula ABX_3 (A and B are cations and X is a halogen ion), the ions are arranged in a crystal lattice so that the B-site cation is surrounded by six nearest neighbor X anions and the A site cation is located inside the cavity formed by eight corner sharing BX_6 octahedra (Fig. 2a). The probability that an ABX_3 compound will form a perovskite crystal is related to the sizes of the A, B, and X ions. This is commonly expressed in terms of two parameters: (1) "tolerance factor, (t)" where $t = (r_A + r_X)/[\sqrt{2(r_B + r_X)}]$; (2)
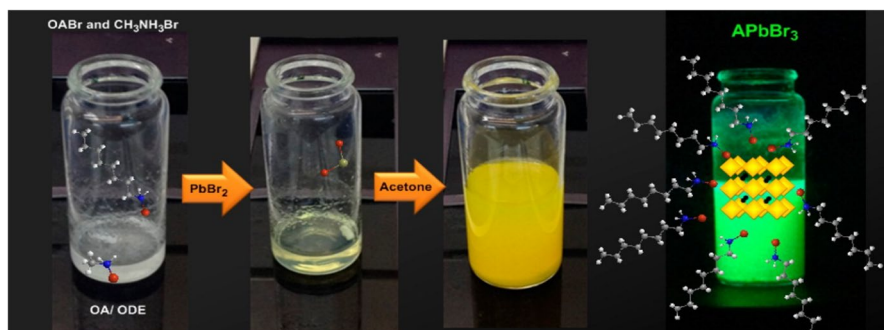
Fig. 1 The conventional solution-based synthesis of hybrid perovskite nanoparticles. The green emission of the final product confirms the formation of highly emissive MAPbBr$_3$ NCs. Reproduced with permission from ref. [23]. Copyright 2014 American Chemical Society
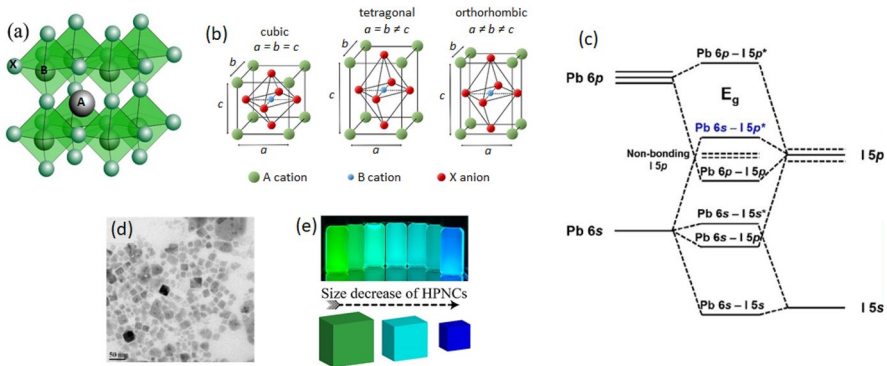
Fig. 2 **a** Three-dimensional (3D) metal halide perovskite structure. In the figure, the green spheres represent halogen atom and black sphere represent organic/inorganic cation sites, inside the eight-corner sharing BX_6 octahedra. The spheres inside the octahedra represent the B atoms. **b** Various crystal phases adopted by $MAPbI_3$ HP. Adopted from ref. [27]. **c** Molecular orbital diagram for the interaction between the B-site metal atoms and the X-site halogen atoms. Reproduced with permission from ref. [28]. **d** TEM image of $CsPbBr_3$ HPNCs. **e** Depiction of the effect of the quantum confinement effect on the photoluminescence of the ABX_3 nano cubes

"octahedral factor, (μ)" where $\mu = r_B/r_X$. Here r_A, r_B, and r_X are the ionic radii of the A, B, and X ions, respectively. The compound that forms a perovskite phase typically meets the conditions: $\mu \geq 0.41$ and $0.8 < t < 1.0$ [24, 25]. Depending on the type of the A cation, HPs can be categorized into: (a) organic HPs, where A is methylammonium (MA), formamidinium (FA), or other monovalent organic cation or (b) inorganic HPs, where A is Cs^+, Rb^+, or other monovalent inorganic cation. The B site is typically occupied by divalent ions such as Pb^{2+}, Sn^{2+}, or Ge^{2+}. X is halogen anion, such as Cl^-, Br^-, or I^-. Depending on the temperature, HPs can adopt multiple crystal phases with different symmetry (Fig. 2b). The most studied HP, $MAPbI_3$, forms, in a temperature range of 160–330 K, a tetragonal phase where two of the unit cell lengths are equivalent ($a = b \neq c$) [26, 27]. At temperatures below 160 K, it forms an orthorhombic structure where all three unit cell lengths are different ($a \neq b \neq c$). At temperatures above 330 K, the symmetry of the structure increases, with $MAPbI_3$ adopting the cubic crystal structure ($a = b = c$) [26]. The electronic structure of the bulk HPs is mainly dictated by the extent of mixing of the B cation's and X anion's "s" and "p" orbitals (Fig. 2c) [28]. As a result, the optical properties of the HP can be effectively tuned throughout the visible spectral range by partial or complete substitution of the halogen ion. The above principles generally apply to the HPNCs as well. However, when the size of the HP is reduced to the nanoscale level, the electronic structure, optical, and electronic properties are further affected by the size of the NCs due to the quantum confinement effect (Fig. 2d, e). The effects of quantum confinement on the optical properties of HPNCs are discussed in more detail in following sections.

3 Synthetic Strategies for Preparation of HPNCs

3.1 Reprecipitation Method

"Reprecipitation" is an old synthesis method that was first used in the production of crystalline salts in clay pots in south Poland as early as 3500 BC [29]. In this process, ionic compounds are typically dissolved in a suitable solvent until the saturation limit is achieved. The saturated solution is then rapidly transferred into another solvent, in which the ionic compound has a low solubility. This leads to instantaneous reprecipitation and initiation of the crystallization, which continues until the system reaches a thermodynamic equilibrium. This method has been used successfully in the preparation of many crystalline compounds and polymers [30, 31]. In 2012, Papavassiliou et al. [32] reported the first synthesis of hybrid HP via reprecipitation method. $(CH_3NH_3)(C_4H_9NH_3)_2Pb_2X_7$, (CH_3NH_3) $(CH_3C_6H_4CH_2NH_3)_2Pb_2X_7$, and $CH_3NH_3PbX_3$, $(X=Cl^-, Br^-, or I^-)$ with the electronic structure of the bulk material were synthesized by a procedure, where a saturated solution of the precursor salts were first prepared in a highly polar solvent [e.g., dimethylformamide (DMF)], and this solution was subsequently added drop-wise into a nonpolar solvent (e.g., toluene). This led to a rapid precipitation of the HP crystals. Few years later, hybrid ($MAPbX_3$) HPNCs were prepared by the reprecipitation method [33]. The method was further extended to the preparation of other mixed HPNCs, with composition ABX_3, where A is MA^+, FA^+, or Cs^+, B is Pb^{2+} or Sn^{2+}, and X is Cl^-, Br^-, or I^-.[34]

### 3.2 Ligand-Assisted Reprecipitation (LARP)

When the reprecipitation is done in the presence of ambipolar compounds (surface ligands), which adsorb onto the surfaces of the forming crystals during their growth and help optimize their size, and shape, the method is known as the "ligand-assisted reprecipitation" (LARP). Schmidt et al. [23] were the first to report the solution-based synthesis of $MAPbBr_3$ HPNCs in the presence of ligands. In the synthesis, long-chain ammonium bromide salt with an organic acid was heated (80 °C) in an organic solvent [1-octadecene (1-ODE)]. The subsequent addition of perovskite precursors ($PbBr_2$ and MABr, predissolved in DMF) produced a yellow dispersion, from which the HPNCs immediately precipitated out upon the addition of acetone. The first successful synthesis of various halide hybrid perovskite QDs by the LARP method was reported by Zhang et al. in 2015 [33]. The approach is schematically summarized in Fig. 3a–c. In the process, perovskite precursors (PbX_2 and MAX, where X is Cl^-, Br^-, or I^-) are dissolved in a highly polar solvent (DMF), which is followed by an addition of a long-chain amine (e.g., n-octylamine) and an organic acid (e.g., oleic acid). Then, the solution is dropped into vigorously stirred toluene, which leads to the formation of HPNCs. This method was successfully used in the preparation of HPNCs with various halogen compositions and tailored emission properties over the visible spectral range, as shown in Fig. 3d and e. Authors found,
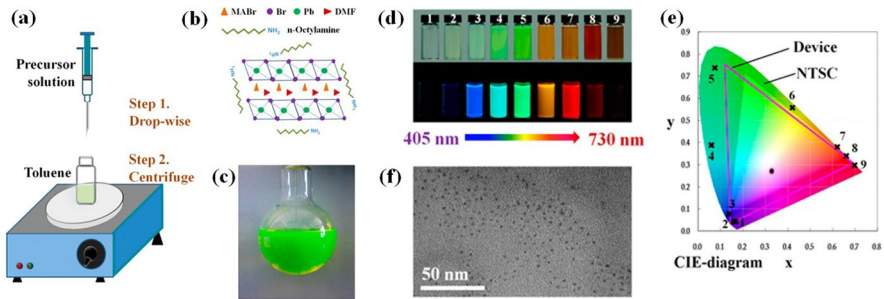
Fig. 3 **a** Schematic illustration of the LARP reaction process. Drop-wise addition of a perovskite precursor solution in a polar solvent, such as DMF, into a nonpolar solvent, such as toluene, leads to instantaneous precipitation of the perovskite NPs. **b** Summary of the starting materials used in the precursor solution. **c** A photograph of the colloidal MAPbBr$_3$ solution prepared in step 1 of the LARP process. **d** Digital images of various MAPbX$_3$ (X is Cl$^-$, Br$^-$, I$^-$) NCs under ambient light (top) and a 365 nm UV lamp (bottom). **e** CIE map indicating the characteristics of various prepared MAPbX$_3$ QDs. **f** TEM image of MAPbBr$_3$ NCs. Reproduced with permission from Ref. [33]. Copyright 2015 American Chemical Society

that in the absence of ligands, such as *n*-octylamine, the crystallization is faster, leading to aggregation of the NCs. In addition, it was determined that the addition of oleic acid leads to a significant improvement of the photoluminescence (PL) stability of the prepared HPNCs. In the absence of oleic acid, the reaction yields HPNCs, which rapidly lose emissivity. Thus, oleic acid has multiple functions: it prevents aggregation of HPNCs, improves their chemical stability, and stabilizes their PL. TEM images of the HPNCs prepared by this method are shown in Fig. 3f. In 2016, Levchuk et al. [35] utilized LARP method to synthesize FAPbX$_3$ NCs. The synthesis protocol used was the same as discussed above, except the FAX (FA is CH$_5$N$_3^+$ and X is Cl$^-$, Br$^-$, or I$^-$) was substituted with MAX as the perovskite precursor. The significant difference, however, was the use of chloroform, instead of toluene, as the antisolvent for the precipitation of FAPbX$_3$ HPNCs. Synthesis in toluene did not result in the formation of FAPbI$_3$ NCs, while FAPbBr$_3$ or FAPbCl$_3$ immediately formed a turbid suspension of large particles and agglomerates. Similarly, in 2016, Li et al. [36] showed that CsPbX$_3$ HPNCs could also be produced using the LARP approach at room temperature by merely replacing MAX with CsX. It was found that not only hybrid or inorganic perovskite but also other kinds of lead-free perovskites could be synthesized by this method.

Leng et al. [37] synthesized vacancy-ordered triple halide perovskite, i.e., MA$_3$Bi$_2$X$_9$ (X is Cl$^-$, Br$^-$, or I$^-$) HPNCs by the LARP method. The authors showed that for these nonstandard HPNCs they could tune the NC emission from 360 to 540 nm by varying the halogen composition from Cl$^-$ to I via Br and also achieve ~12% PLQY. The same research group also developed a similar method for synthesis of Cs$_3$Bi$_2$X$_9$ perovskites [38, 39]. Since it was found that BiBr$_3$ is only partially soluble in toluene, to fabricate vacancy-ordered triple halide perovskites instead of toluene, octane was used as a "poor solvent" to reprecipitate the HPNCs. In 2017, Zhang et al. [40] showed that more exotic perovskite structures, such as Cs$_3$Sb$_2$Br$_9$, can also be effectively synthesized by the LARP method. They used this
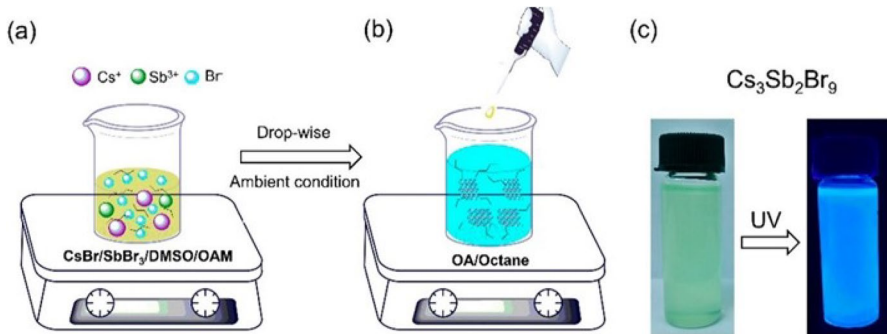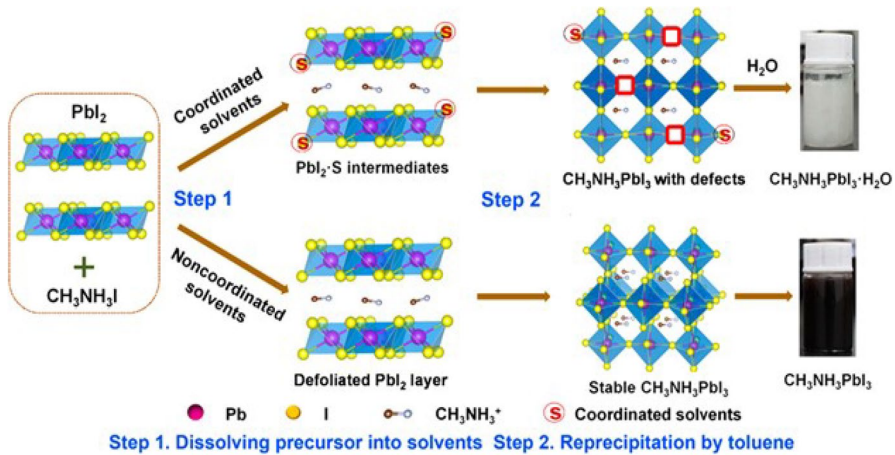
Fig. 4 **a**, **b** Schematic illustration of the reaction process for LARP based chemical synthesis technique for $Cs_3Sb_2Br_9$ NPs. **c** Digital images of a $Cs_3Sb_2Br_9$ NPs colloidal solution with and without 365 nm UV light excitation. Reproduced with permission from ref. [40]. Copyright 2017 American Chemical Society

method to fabricate blue-emitting $Cs_3Sb_2Br_9$ perovskite QDs (Fig. 4) with ~46% PLQY at 410 nm. The above examples illustrate that LARP is a convenient and versatile method for preparation of HPNCs. Perovskite NCs with various shapes, sizes, and halogen compositions can be prepared with a simple chemical setup at room temperature. Moreover, LARP is a convenient method for preparation of HPNCs ranging from hybrid to inorganic to alternative perovskite structures (e.g., vacancy-ordered triple halide perovskite, double-perovskite etc.), to structures with mixed halogen compositions. However, the method also has several important drawbacks. In the initial step, highly polar organic solvents, such as DMF/dimethyl sulfoxide (DMSO; "good" solvents) are typically used to effectively dissolve various polar precursors. Even after the recovery of the HPNCs with a nonpolar ("poor") solvent, the product NCs will usually retain some polar solvent molecules on their surface. The remains of the polar solvents tend to chemically interact with and gradually degrade the freshly formed NPNCs. Zhang et al. [41] have studied the effect of solvent during the synthesis of $MAPbI_3$ NCs. On the basis of Lewis acid–base theory, the authors proposed that the interaction between the DMF/DMSO (coordinating solvents) and the HPNCs precursor PbI_2 led to the formation of lead oxide (PbO) as shown schematically in Fig. 5. During the recovery of the HPNCs in nonpolar solvent (toluene), in the open air the authors observed formation of white flocculent precipitate of $MAPbI_3 \cdot H_2O$. Thus, the interaction between the PbI_2 and DMF initially creates iodine vacancies associated with the formation of PbO, which in the presence of moisture from air or solvent subsequently transform into $MAPbI_3 \cdot H_2O$, which eventually degrades the perovskite structure.

3.3 Hot-Injection Method

The hot-injection method was first introduced by Murray et al. [42] in 1993 for the synthesis of cadmium chalcogenide NCs. Rapid injection of organometallic precursor(s) into a hot-solution (> 150 °C) of a high boiling point solvent [(e.g., trioctylphospineoxide (TOPO)], was shown to be a very effective method for

Fig. 5 Effect of solvent on the crystal structure of MAPbI$_3$ NCs. Schematic illustration of the MAPbI$_3$ formation from MAI and PbI$_2$ in coordinating solvents (top) and noncoordinating solvents (bottom). Reproduced with permission from ref. [41]. Copyright 2017 American Chemical Society

preparation of CdE (*E* is sulfur, selenium, or tellurium) NCs with narrow (< 10%) size dispersions [43]. This is a result of a high control of the nucleation and growth that this approach allows at various stages of the reaction. A rapid injection of a precursor leads to supersaturation of the hot solution by the monomers, followed by a quick nucleation (formation of small NC nuclei) and a subsequent slower NC growth process. The size and shape of the NCs can be effectively controlled via adjustment in the reaction time and temperature, choice of ligands, solvents, etc.

In 2015, Protesescu et al. [44] used for the first time the hot-injection method for the preparation of HPNCs with compositions CsPbX$_3$, where *X* is Cl$^-$, Br$^-$, or I$^-$. The experimental setup and conditions are schematically shown in Fig. 6a. The HPNCs prepared by the hot-injection method remain stable in terms of their composition and optical properties for a longer period of time (2–3 months) than NCs prepared by the LARP method (few weeks). This has been attributed mostly to the absence of a polar solvents in the hot-injection method. In a typical synthesis of CsPbX$_3$ (*X* is Cl$^-$, Br$^-$, or I$^-$), first, Cs-oleate was prepared by reaction of Cs$_2$CO$_3$ with oleic acid in 1-octadecene (1-ODE) at 120 °C with vigorous stirring. Separately, PbX$_2$ (*X* is Cl$^-$, Br$^-$, or I$^-$) and oleic acid (OA) and oleylamine (OAm) were dissolved in 1-ODE and heated up to 140 °C, while being stirred. The reaction yielded Pb-oleates and free X$^-$ ions. Rapid injection of Cs-oleate into the hot Pb-solution, followed by rapid (4–10 s) reaction quenching with an ice bath led to the formation of CsPbX$_3$ NCs. The amounts of organic amines, carboxylic acids, and temperature were shown to play a critical role in controlling the shape and size of the NCs. Rapid quenching of the reaction after the injection of Cs-oleate into the Pb and halogen precursor helped to achieve uniformity in the shape, as shown in Fig. 6b. In addition, the halogen composition (from I$^-$ to Br$^-$ to Cl$^-$) in CsPbX$_3$ was controlled simply by taking the appropriate ratios of PbX$_2$ salts, allowing production of HPNCs with PL tunability across the entire visible spectrum (410–700 nm), as
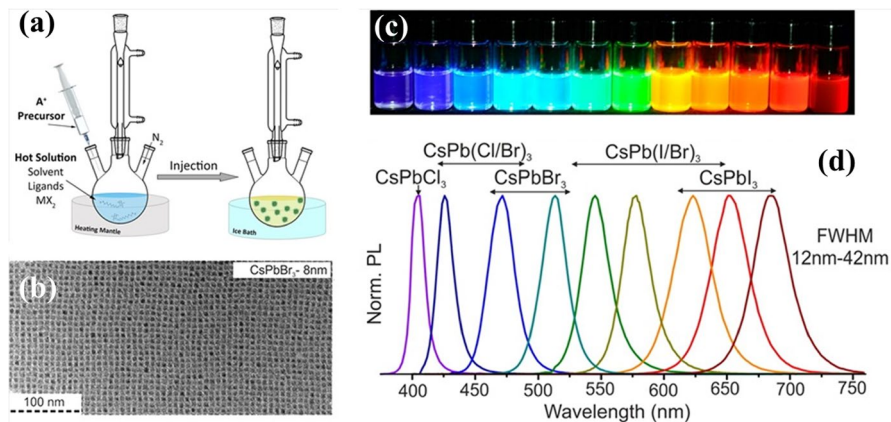
Fig. 6 **a** Schematic diagram of the hot-injection method used for the synthesis of HPNCs. **b** TEM image of monodispersed $CsPbBr_3$ nanoparticles obtained using the hot-injection method. **c** Digital image of $CsPbX_3$ (X is Cl, Br, or I) nanoparticles dispersions (different halide composition in each vial) in toluene under an ultraviolet (UV) lamp ($\lambda = 365$ nm). **d** PL emission spectra of $CsPbX_3$ perovskite NPs with different halogen compositions. PL emission covers the entire visible spectrum (410–700 nm). Reproduced with permission from ref. [44] Copyright 2015 American Chemical Society

shown in the Fig. 6c–d. The hot-injection approach was also used in the synthesis of less typical HPNCs. For example, Akkerman et al. [45] used this method to prepare Cs_4PbBr_6 NCs by adding an excess amount of the Cs-oleate precursor. Similarly, an excess of $PbBr_2$ was shown to yield $CsPb_2Br_5$ PNCs [46]. Furthermore, a modified hot-injection approach was adopted by Protesescu et al. [47] for the colloidal synthesis of $FAPbBr_3$ PNCs by replacing Cs-oleate with FA-oleate. Lignos et al. [48] extended this approach to the synthesis of mixed-halide $FAPb(Cl_{1-x}Br_x)_3$ HPNCs, with a stable blue PL emission. In a separate study, $FAPb(I_{1-x}Br_x)_3$ HPNCs with PL tunable from 570 to 780 nm and $Cs_{1-x}FA_xPbI_3$ PNCs with a controlled emission from 690 to 780 nm were prepared by Protesescu et al. [49] using a similar methodology. With these and other advances, the hot-injection method has been now well established as a standard approach for preparation of HPNCs ranging from 3D-$CsPbX_3$ to 2D-$CsPb_2Br_5$ and 0D-Cs_4PbBr_6. This method can also be used for synthesis of FA-based hybrid HPNCs, with compositions ranging from Cl^- to Br^- to I^-, with range of sizes and shapes. Until 2015, no report has shown full range halogen composition-controlled synthesis of structurally stable MA^+-based hybrid halide perovskite $MAPbX_3$ (X is I^-, Br^-, or Cl^- along with I/Br and Br/Cl mixed halide) via the hot-injection method. This is because, in contrast to Cs^+ and FA^+ precursors, the MA-oleate is difficult to prepare, as MA-acetate is not readily available. This made $MAPbX_3$ synthesis, via the conventional hot-injection method difficult. In addition, MA^+ is volatile in ambient conditions as its boiling temperature is 4 °C. Hence, this molecule is typically stored under THF or alcohols, (e.g., methanol or ethanol) with boiling point in the 60–70 °C range. In 2015, Vybornyi et al. [50] used a modified hot-injection method to synthesize $MAPbX_3$, where X is I^- or Br^- only. In this approach, the PbX_2 was first dissolved, together with organic acid and

amine, in 1-ODE heated to 120 °C. Subsequently, after dissolving the temperature was decreased to ~60–50 °C to reduce the risk of MA^+ decomposition or evaporation. Injection of MA^+ led to rapid formation of $MAPbX_3$ (X is Br^- or I^-). Although the synthesis of Br or I-based HPNCs was successful, the method was not effective in producing mixed compositions with I/Br and Br/Cl. In 2018, Imran et al. [51] reported a "three-precursor" hot-injection method for the synthesis of HPNCs. This novel approach was based on using benzoyl halides (C_7H_5OX, X is Cl^-, Br^-, or I^-) as sources of halogen and lead oxide (PbO) as a source of lead ions, instead of the conventional reaction of PbX_2 (X is Cl^-, Br^-, or I^-) salts with MA molecule (in THF). Separation of the source of the lead and the halogen into two compounds provided a better control over the relative amounts of the ions in the reaction and, thus, finer tunability of the reaction conditions. In a typical synthesis, the PbO and organic ligands were heated in 1-ODE at 125 °C to solubilize the salts. Subsequently, the temperature was lowered to 65 °C, and MAX was injected, followed by the injection of the benzoyl halide. This approach was successfully used in preparation of $APbX_3$ (A is Cs^+, MA^+, or FA^+ and X is Cl^-, Br^-, or I^-) NCs. In spite of these important advances, the "two-precursor"-based hot-injection synthesis of composition-controlled MA-based hybrid HPNCs has been lacking. In 2019 Roy et al. [52] used a modified hot-injection method by including TOP in the reaction to enhance the solubility of PbX_2 in 1-ODE. They used "two-precursor"-based hot-injection method to successfully synthesize all composition-controlled MA-based HPNCs, without the need to use polar solvent or any specialty precursor. On the other side TOPO/TOP classical ligands, which are used to synthesis traditional chalcogenide nanocrystals, are also used in perovskite synthesis to stabilize the perovskite structure. In 2017 Liu et al. [53] reported use of $TOP-PbI_2$ as precursor for synthesis of $CsPbI_3$ NC synthesis via the hot-injection method. In this method presynthesized $TOP-PbI_2$ was injected into the reaction mixture of Cs_2CO_3, oleic acid, and oleylamine in ODE. They are also able to tune the size of the NC by varying the reaction temperature. They confirm that the use of TOP leads to higher structural stability and enhanced the PLQY by comparing non-TOP caped $CsPbI_3$ NCs. In another example, Wu et al. [54] use TOPO along with oleic acid and oleylamine to synthesis $CsPbBr_3$ NCs in the hot-injection method. Use of TOPO leads to monodisperse $CsPbBr_3$ nanocubes at high temperature, i.e., 260 °C. These TOPO caped NCs exhibited superior stability in ethanol as compared with that of OA/OAm-capped $CsPbBr_3$ nanocubes, regardless of the reaction temperatures at which they were synthesized.

3.4 Less Conventional Approaches

The development of the hot-injection and LARP methods allowed for preparation of HPNCs with broad range compositions. Hot injection is very effective method for controlling the HPNC composition, size, and shape, along with the size and shape dispersion in small-scale reactions. Due to the limited stability of HPNCs at ambient conditions, the hot-injection method requires use of strictly anhydrous solvents and inert atmosphere. This means that a relatively complex chemical apparatus must be used, and the syntheses are more time consuming compared with the LARP method.

In addition, due to the injection step, the hot-injection method is difficult to scale up to the commercial production scales. Increase in the quantities of the precursor at high temperatures leads to inhomogeneous nucleation and growth, which makes it difficult to control the shape and size of the HPNCs in a large-scale reaction. In addition, using the hot-injection method it is often difficult to produce halogen rich HPNCs, which were shown to have the most desirable PL properties [55]. To address these challenges, several alternative methods were developed to simplify the preparation of composition-controlled HPNCs. These methods are described in the following sections.

3.4.1 Solvothermal Synthesis

One of the methods proposed as an alternative to the hot-injection or LARP approach is solvothermal synthesis. Chen et al. [56] developed a simple solvothermal method for the preparation of HPNCs with uniform halogen composition. In a typical synthesis, cesium acetate and lead halides are mixed in a stainless autoclave containing 1-ODE, with an organic acid and amines. The autoclave is placed in an oven and heated to 160 °C for 30 min. The reaction leads to the formation of composition-controlled $CsPbX_3$ (X is Cl^-, Br^-, or I^-, along with mixed halides) nanocubes, with PL tunable throughout the visible range. The method provides means not only for tuning of the composition and PL energy but also for morphology of the HPNCs. While the lower initial concentration of the precursors leads to formation of cubic HPNCs, higher precursor concentrations lead to formation of HP Nanorods (HPNRs). Parveen et al. [57] extended this method to the hybrid HPNCs ($MAPbX_3$). In this variation, the amine/acid to precursor ratios were systematically varied to control the size of the NCs. The quantum confinement effects were seen and a systematic shift in the emission peak position is observed from green to blue.

3.4.2 Synthesis Using Microwave Radiation

In 2017, Pan et al. [58] described a new strategy for synthesis of HPNCs using microwave radiation. Cesium acetate (Cs-OAc), lead halide, organic ligands, trioctylphosphine oxide (TOPO), and 1-ODE were mixed together in a quartz tube and transferred into a microwave reactor. Heating the reaction mixture to 160 °C by microwave radiation led to formation of the $CsPbX_3$ HPNCs. This method also allows for control of the halogen composition and the morphology of the HPNCs. The authors of the study found that the shape of the $CsPbBr_3$ NCs varies from nanocubes to a nanoplatelets (NPLs) with change in the reaction temperature from 160 °C to 80 °C. It is also noted that rod-shaped $CsPbBr_3$ HPNRs s can be prepared when the precursors are predissolved prior to the microwave treatment. Shamsi et al. [59] modified the microwave assisted method to prepare blue emitting quantum confined $CsPbBr_3$ NCs. More recently, Liu et al. [60] further extended this approach and formulated a general strategy for synthesis of low-dimensional $CsPbBr_3$ NPs with morphology tunable from QDs to NRs to NPLs. This was achieved by simple adjustment in the ratios of the oleic acid to oleylamine and 1-ODE to diethylene glycol butyl ether (DGBE) and careful variations in the concentration of $PbBr_2$.

Together, with the dimensional/morphological changes, the size of the HPNCs could also be optimized by a simple change of the applied microwave power.

3.4.3 Synthesis by Ultrasonication

Jang et al. [61]. reported the preparation of $CsPbX_3$ (X is Cl^-, Br^-, or I^-) and their mixed compositions by ultrasonication. In this approach, ultrasonic irradiation is used to accelerate dissolution of the precursors (AX and PbX_2) in nonpolar solvent, such as toluene, and to control the growth rate of the HPNCs. The prolonged sonication was shown to lead to formation of HP nanowires (HPNWs). A similar approach reported by Tong et al. [62] for preparation of $CsPbX_3$ NCs and the characterization of the prepared materials are graphically summarized in Fig. 7. As illustrated in the figure, the method provides a good control over the halogen composition as well as the optical properties of the Cs^+, MA^+, and FA^+-based HPNCs. More recently, Roy et al. [63] developed a method based on ultra-sonication, which allows for control of the halogen composition in already phase-formed HPNCs, exploiting the significant ionic mobility and low activation energy for the ion exchange in these materials. In this method, two compositions of HPNCs ($MAPbX_3$ and $MAPbY_3$) are mixed together in a nonpolar solvent (e.g., toluene) and exposed to ultrasound waves. Upon sonic energy exposure, the X^- and Y^- ions migrate from one HPNC structure to another to ultimately form mixed composition $MAPb(X/Y)_3$. Thus, this method allows for a straightforward preparation of HPNCs with specific mixed
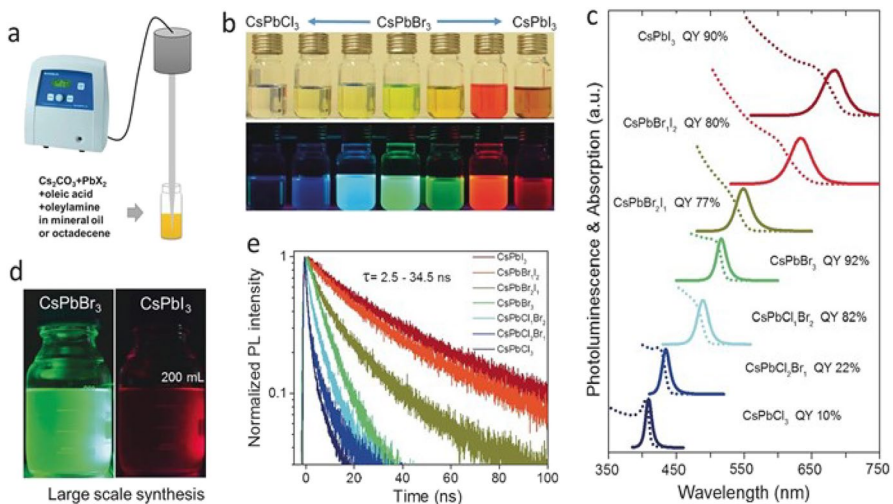
Fig. 7 a Scheme of the experiment used in the synthesis of the $CsPbX_3$ NCs via the ultrasonication method. **b** Digital image of perovskite NCs with various halogen (X is Cl^-, Br^-, or I^-) composition in hexane under visible light (top) and UV light (bottom, $\lambda = 367$ nm). **c** Absorption and emission spectra with the PLQY values of the HPNCs. **d** Products of large-scale synthesis of HPNCs. **e** PL decay dynamics of the HPNCs ($\tau \approx 2.5$–34.5 ns). Reproduced with permission from Ref. [62]. Copyright 2016 Willy
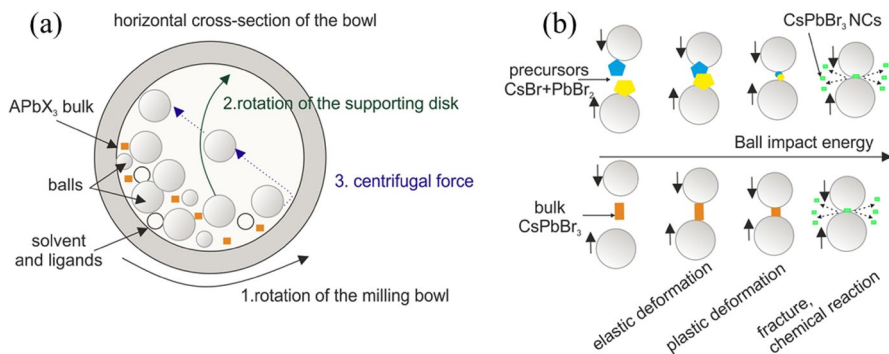
Fig. 8 Schematic diagram of **a** Working principle of the planetary ball-mill grinding. **b** Various stages of the planetary ball-mill grinding process during the mechanochemical synthesis of perovskite NPs. Reproduced with permission from Ref. [69]. Copyright 2018 American Chemical Society
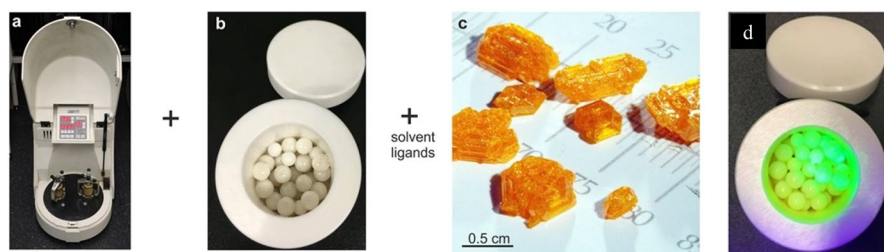
Fig. 9 Digital photographs of **a** a ball mill machine, **b** zirconia bowl filled with zirconia balls, **c** bulk CsPbBr$_3$ used as a starting material. **d** Highly emissive HPNCs produced by the ball-milling process. Reproduced with permission from ref. [69]. Copyright 2018 American Chemical Society
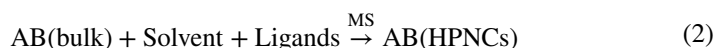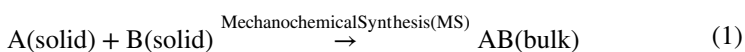
halide compositions by appropriate stoichiometric mixing of the phase pure single halogen NCs, followed by a brief period of ultrasonication.

3.4.4 Mechanochemical Methods

In addition to wet chemical routes, described in previous sections, HPNCs can also be prepared by mechanochemical methods. Mechanochemistry refers to the branch of chemistry where the energy necessary to drive the chemical reaction is provided by a mechanical force (Figs. 8 and 9). The mechanochemical synthesis offers several advantages. The process is entirely solvent-free (or uses small amounts of volatile solvents), which makes it convenient for scale up to industrial production. In addition, the published reports indicate [64, 65] that the mechanochemically synthesized perovskite compounds have better chemical stability than the HPNCs prepared by the conventional polar solvent-based methods. Mechanochemical synthesis of HPNCs is typically carried out either by hand-grinding of the perovskite precursors with mortar-pestle or via ball milling. In a typical synthesis, a stoichiometric amount of the perovskite precursors (AX and PbX$_2$)

and long chain ammonium halide salts are transferred into a mortar and ground by hand with a pestle. While hand grinding of perovskite precursors is a simple and convenient approach for preparation of HPNCs, it is also quite tedious and, more importantly, typically leads to formation HPNCs with structural defects. Therefore, a powder ball-milling is often used as an alternative. In this approach, PS precursors are first loaded into a stainless-steel jar, together with several balls made of a high hardness material such as zirconia, corundum, or agate. The balls serve as the grinding medium. The steel jar is transferred into a rotor providing the mechanical energy. The energy provided by rotor is transferred to the reagents by the grinding balls by compression, shear, and/or friction.

Mechanochemical synthesis methods can be subdivided into two approaches. In the first approach, there are two steps, as shown in Eqs. (1) and (2): (1) synthesis of bulk PS by mechanochemical method and (2) reduction of the size of the bulk PS by the mechanochemical method in the presence of a volatile solvent and surface-capping ligand molecules.

$$A(solid) + B(solid) \xrightarrow{Mechanochemical Synthesis (MS)} AB(bulk) \tag{1}$$

$$AB(bulk) + Solvent + Ligands \xrightarrow{MS} AB(HPNCs) \tag{2}$$

The second approach is a direct synthesis of HPNCs from the appropriate precursors in the presence of a solvent and ligands, as shown in Eq. (3):

$$A(solid) + B(solid) + solvent + ligands \xrightarrow{MS} AB(HPNCs) \tag{3}$$

In 2016, Hintermayr et al. [66] prepared $MAPbX_3$ (X is I^-, Br^-, Cl^-, and their mixtures) NCs by two-step mechanochemical synthesis. In the first step, the bulk PS was prepared by hand grinding an equal amount of MAX and PbX_2 with a mortar-pestle method. This was followed by sonication of the reaction mixture in toluene in the presence of ligands. The synthesis yielded HPNCs with controlled chemical composition and PL energies. In this case, the second synthesis step did not involve any mechanical milling. Instead, the ultrasonication was used as an alternative. Zhu et al. [67] followed a two-step approach for the synthesis of fully inorganic $CsPbX_3$ HPNCs. In the synthesis, the dry ball-milling step was applied first to produce the desired perovskite compound in a bulk form. In a second step, the product was further milled in a presence of a small amounts of organic ligands, with no added solvent. Authors showed that by this method it is possible to effectively tune the composition of the resulting HPNCs. This method also allows for preparation of HPNCs by grinding of the binary halide precursors directly in wet conditions, i.e., in the presence of solvent and ligands, sometime referred to as liquid-assisted grinding (LAG) [68]. Protesescu et al. [69] used this method to synthesize hybrid as well as inorganic ($FAPbBr_3$ and $CsPbBr_3$) HPNCs and showed that composition of the perovskites in $CsPb(Br/I)_3$ can be varied through a mechanically induced anion-exchange process. They also demonstrated that prolonged milling causes a blue shift in the PL spectra, which was attributed

to the formation of quantum confined HPNCs. Chen et al. [70] extended this method to synthesis of broad range of HPNCs from MA^+ to FA^+ to Cs^+ HPNCs with the range of halogen compositions (Table 1).

4 Composition Modification by Ion Exchange

Controlled exchange of ions at A-, B- or X-sites of the HPNC is an effective method for the preparation of NCs with desired chemical compositions and means for tuning the stability, optical, and properties of HPNCs. The postsynthesis HPNC composition modification by ion exchange was recently covered in several comprehensive reviews [72–74]. In short, substitution at the A-site can lead to enhanced phase stability of the PS related to the change in the tolerance factor. Similarly, B-site doping can also increase the PS stability by modification of the B–X bond length, whereas the X-site substitution is primarily used to modify the bandgap of the HPNCs. We note that this oversimplified generalization, while conceptually useful, is not entirely accurate in describing all the effects of the dopant ions in the HPNCs. Various ion substitutions often lead to more subtle variations in the band alignment, PL energy, or carrier mobilities etc. Partial substitution of the B-site cation was shown to be thermodynamically less favorable than the substitution of ions at the A and X sites, because of the larger formation energy of the former [75]. Based on theory, [52] the conduction band of ABX_3 perovskites is mainly composed of Pb^{2+} 6p orbitals, with a minor contribution from X^- ns orbitals ($n = 5, 4,$ and 3 for I^-, Br^-, and Cl^-, respectively), whereas the valence band is primarily comprised of Pb^{2+} 6p–X ns antibonding states. As a result, the electronic band gap of HPs is not significantly affected

Table 1 Synthetic methods used in preparation of bulk HPNCs

| Perovskite type	Synthesis method	Shape	References
$CsPbX_3$ (X is Cl, Br, or I)	Hot-injection method	NCs	[44]
$MAPbBr_3$ (X is Cl, Br, or I)	Hot-injection method	NPLs	[50, 51]
$FAPbBr_3$	Hot-injection method	NCs	[35]
$MAPbX_3$ (X is Cl, Br, or I)	LARP Method	QDs	[23, 33]
$CsPbX_3$ (X is Cl, Br, or I)	LARP Method	NCs	[36]
$FAPbX_3$ (X is Cl, Br, or I)	LARP Method	NCs	[35]
Layered halide perovskite $\grave{A}_2A_{n+1}Pb_nBr_{3n+1}$ (A is MA and À is organic alkylammonium cations)	LARP Method	NPLs	[71]
$CsPbX_3$ (X = Cl, Br, I)	Solvothermal method	NCs, NRs	[56]
$MAPbX_3$ (X is Cl, Br, or I)	Solvothermal method	Nanosheets	[57]
$CsPbX_3$ (X = Cl, Br, I)	Microwave radiation	NCs, NPLs, NWs	[58]
$APbX_3$ (X is Cl, Br, or I; A is MA, FA, or Cs)	Ultrasonication	NCs	[61]
$CsPbX_3$ (X is Cl, Br, or I)	Ultrasonication	NCs, NPLs	[62]
$CsPbX_3$ (X is Cl, Br, or I)	Mechanochemical	NCs	[67, 69]

The references include only the first publication of a given method

by the A^+ cations, but a direct substitution of the B-site cation leads to dramatic changes in the electronic structure of HPNCs and their optical and electronic properties. On the other hand, removal of any atom from the lattice leads to formation of point defects. Various experimental observations indicate that defects due to halogen vacancy and B-site defects lead to reduced PLQY. In contrast, the vacancies or substitutions at the organic/inorganic A-site do not significantly affect the HP electronic structure or optical properties. However, they do affect the chemical and thermal stability of the HP thin films and NCs [76]. Due to its prominent effect on the electronic structure of the HPNCs and its potential to address the Pb-associated toxicity of the HPNCs, in the following sections we review most common approaches used in B-site substitution and the effect they have on the electronic properties of HPNCs. For a detailed overview of the methods used for A- and X-site ion exchanges and the effects of these substitutions on the properties of HPNCs, we refer the reader to the recent comprehensive reviews dedicated to this topic [72, 73].

4.1 Homovalent B-Site Ion Exchange

The main motivation in search for effective strategies for the B-site substitution is the reduction of the toxic lead content. The tin (Sn^{2+}) ion has so far been the most explored because of its low toxicity and chemical similarity with Pb^{2+} [77, 78]. Both partial and a complete substitution of Pb^{2+} by Sn^{2+} were demonstrated [79, 80]. In one example, Zhang et al. [81] synthesized Sn^{2+}-doped $CsPbBr_3$ NCs by the hot-injection method. In this synthesis, stoichiometric amount of $PbBr_2$ and $SnBr_2$ were taken in 1-ODE, along with equal ratio of OA and OAm, and heated to 100 ℃, followed by addition of cesium stearate at ~140 ℃, which led to the formation of Sn-doped $CsPbBr_3$ NCs. A blue shift in the absorption edge from 520 to 496 nm, along with a blue shift in the PL peak, was observed, correlating with the increase in the Sn^{2+} content in the structure (Fig. 10a, b). It was also shown that with increasing Sn^{2+} content the PLQY decreases (71–37%). Deng et al. [82] synthesized Sn^{2+}-doped $CsPbBr_3$ NCs via the LARP method [82]. They found that $CsPb_{1-x}Sn_xBr_3$ NCs show enhanced PLQY (for $x = 0.1$), but the PLQY decreased sharply for $x > 0.1$. This suggests that higher content of Sn^{2+} leads to formation of defect states and increases the efficiency of the nonradiative excited state relaxation. It was also observed that with increasing concentration of Sn^{2+}, $Cs(Pb^{2+}/Sn^{2+})Br_3$ perovskite gradually converts into $Cs_2Sn^{4+}Br_4$. This is because Sn in its +2-oxidation state is unstable under ambient conditions, spontaneously oxidizing into Sn^{4+}. The associated change in the ionic radius destabilizes the perovskite lattice. A complete replacement of Pb^{2+} with Sn^{2+} has also been studied. In 2016, Jellicoe et al. [83] synthesized $CsSnX_3$ (where X is Cl^-, Br^-, I^-, or I^-/Br^- and Br^-/Cl^- mixed halides) HPNCs via the hot-injection method. The conventional hot-injection method used for synthesis of $CsPbX_3$ was unsuccessful in preparation of $CsSnX_3$ and ultimately led to precipitation of CsX. To prevent the formation of CsX and to aid formation of $CsSnX_3$, initially, 1 M stock solution of SnX_2 in the presence of tri-n-octylphosphine (TOP) was prepared at 170℃, and then stock solution is injected into the solution of Cs-oleate, which leads to the formation of $CsSnX_3$ NCs. The electronic structure of
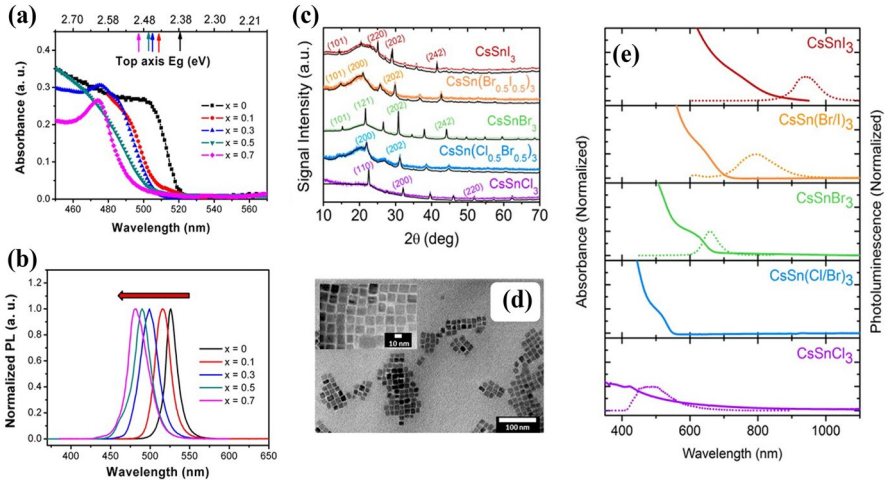
Fig. 10 Steady state **a** absorption and **b** emission spectra of $CsPb_{1-x}Sn_xBr_3$ NCs, where $x = 0$–0.7 and as x increases, the absorption band is blue shifted from 520 nm ($x = 0$) to 496 nm ($x = 0.7$). Reproduced with permission from ref. [81]. Copyright 2016 Elsevier. **c** XRD pattern of $CsSnI_{3-x}Br_x$ perovskite NPs shows that these NPs belong to the orthorhombic phase. **d** TEM image of $CsSnI_3$ perovskite NCs. **e** Steady-state absorption and emission spectra of $CsSnI_{3-x}Br_x$ and $CsSnBr_{3-x}Cl_x$ NCs. Reproduced with permission from ref. [83]. Copyright 2016 American Chemical Society

$CsSnX_3$ NCs was shown to be tunable with absorption and PL ranging from 500 to 900 nm (Fig. 10c–e), depending on the halogen composition. The authors observed that Sn^{2+}-based $ASnX_3$ NCs have smaller bandgap than the Pb^{2+}-based $APbX_3$ NCs. This is due to the higher electronegativity of the Sn^{2+} ions occupying the "B" site in the ABX_3 structure. Although the Sn-based HPs have smaller bandgaps than their Pb-based analogs, they are chemically unstable under the ambient conditions. XPS and PL lifetime investigations revealed that under ambient conditions the Sn-based PSs undergo spontaneous gradual oxidation of Sn from oxidation state +2 to +4. Consequently, the Sn-based PSs have limited practical potential for photovoltaic as well as other optoelectronic applications. In addition, a recent study has also shown that the starting material and the decomposition product SnI_2 are more toxic than PbI_2 [84].

Transition metal doping in semiconductors is widely explored as means for optimization of optical, magnetic, and electronic properties. In the case of lead-based HPNCs, the effect of substitution in the B-site was explored with a broad range of transition metal ions (Co^{2+}, Cu^{2+}, Fe^{2+}, Mg^{2+}, Mn^{2+}, Ni^{2+} Sr^{2+}, Zn^{2+} etc.) [75]. Of the explored metals, the doping with Mn^{2+} was perhaps the most widely studied. Chlorine-based $CsPbCl_3$ is the most suitable material for studies of doping effects, thanks to its relatively wide bandgap, which provides an opportunity for introduction of new intraband states via doping. Parobek et al. [85, 86] and Liu et al. [85, 86] were the first to investigate the doping of Mn^{2+} into $CsPbCl_3$ via the hot-injection approach. In this approach, $MnCl_2$ and $PbCl_2$ were dissolved together in 1-ODE as a solvent at a moderate temperature (160 °C) in the presence of equal amount of organic amine and an acid, such as oleylamine and oleic acid. Then, an

independently prepared Cs-oleate was injected into the precursor mixture solution to initiate the crystallization of the Mn^{2+}-doped $CsPbCl_3$. While the undoped $CsPbCl_3$ has a characteristic narrow PL with peak at ~402 nm, Mn^{2+}-doping leads to observation of a new PL peak at ~586 nm (Fig. 11a–c). The new PL changes the color of the emitted light from blue to bright orange. The low energy excited state of the Mn-doped $CsPbCl_3$ has a long emission life time of ~1.6 ms due to the spin forbidden nature of the $^4T_1$–$^6A_1$ transition [87]. The substitution of the halogen ion from Cl^- to Br^- ions leads to an increase in the PL intensity of the band-to-band transition, while the PL intensity of the peak associated with the Mn^{2+} dopant gradually declines with increasing Br^- content. This observation indicates that the excitonic energy relaxation through the Mn^{2+} dopant states is reduced in the Br-based PSs, which means that the Mn-doping plays a less significant role in the relaxation of excited state in $CsPbBr_3$ than in $CsPbCl_3$ PSs.

In a related study, Stam et al. [88] incorporated Cd^{2+} and Zn^{2+} ions into the $CsPbBr_3$ NCs to tune their optical properties. They initially synthesized $CsPbBr_3$ NCs by method described by Protesescu et al. [44]. Next, 1 mmol of metal bromide salt (MBr_2, with M being Sn^{2+}, Zn^{2+}, or Cd^{2+}) in 10 mL of toluene (0.1 M MBr^2), in the presence of 100 μL of OAm, was prepared. Doping of metal cation was achieved by ion exchange in the presence of 0.5 mL of cation precursor (with concentrations ranging from 0.125 to 1.67 mM), injected into 1.5 mL of diluted NCs in toluene (concentration ~0.01 μM) and mixed and stirred at room temperature for ~16 h. Cd^{2+} or Zn^{2+} doping in $CsPbBr_3$ leads to a blue shift in the absorption and PL spectra, as shown in Fig. 11d–f. PL peak position was tuned from ~452 to ~512 nm by Cd^{2+}-doping and from ~462 to ~512 nm via Zn^{2+}-doping. In both cases the doped NCs showed narrow PL (FWHM ≈ 80 meV) with high PLQYs (> 60%). Shen et al. [89] showed that Zn^{2+} doping in $CsPbI_3$ NCs leads to a small change in the PL energy (690–678 nm), but PLQY increases from 61.3% to 98.5%. Likewise, successful Cu^{2+} doping in $CsPbBr_3$ NCs was reported by Bi et al. [90].
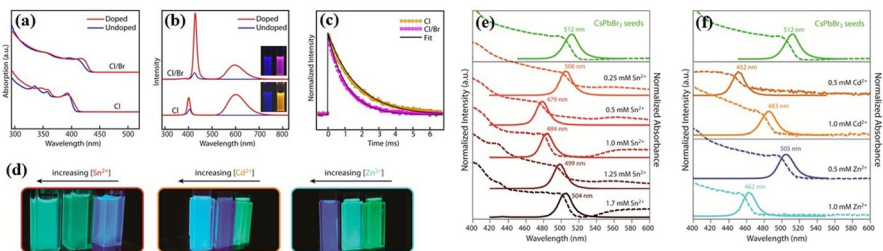
Fig. 11 **a** UV–visible light absorption spectra of Mn:$CsPbCl_3$, $CsPbCl_3$, Mn:CsPb(Cl/Br)$_3$, and CsPb(Cl/Br)$_3$ NCs. **b** PL emission spectra of Mn-doped and undoped $CsPbCl_3$ and CsPb(Cl/Br)$_3$ NCs (inset: digital image of Mn^{2+} doped and undoped perovskite NCs). **c** Emission lifetime of Mn^{2+}-doped and undoped $CsPbCl_3$ and CsPb(Cl/Br)$_3$ NCs. Reproduced with permission from ref. [85]. Copyright 2016 American Chemical Society. **d** Digital image of Sn, Cd, and Zn doped perovskite NCs. **e** Absorption and emission spectra of Sn-doped $CsPbBr_3$ NPs show a change from 512 to 479 nm. **f** Absorption and emission spectra of Cd^{2+} and Zn^{2+} doped $CsPbBr_3$ show a change from 512 to 483 nm and 512 nm to 462 nm, respectively. Reproduced with permission from ref. [88]. Copyright 2016 American Chemical Society

In this report, they used the hot-injection method to synthesize Cu-doped $CsPbBr_3$ NCs. $PbBr_2$ and mixture of copper acetate $Cu(OAc)_2$ and $CuBr_2$ in stoichiometric ratio in 1-ODE, in the presence of oleic acid oleylamine, were heated up to 185 ℃. Previously prepared Cs-oleate was injected into the reaction mixture, resulting in the formation of Cu-doped $CsPbBr_3$. The Cu^{2+} doping was shown to cause a small blue shift in the PL from 517 to 499 nm. The authors also reported enhanced PLQY and improved thermal stability of Cu^{2+}-doped NCs. De et al. [91] also doped Cu^{2+} in the $CsPbCl_3$ NCs. The hot-injection method was used to prepare Cu-doped $CsPbCl_3$ as discussed by Protesescu et al. [44]. $PbCl_2$ and $CuCl_2$ in stoichiometric ratio were dissolved in 1-ODE in the presence TOP and heated up to 185 °C. Previously prepared Cs-oleate was injected into the reaction mixture producing Cu-doped $CsPbCl_3$. The authors found no significant shift in the PL energy but observed an improved PLQY. It was shown that an optimal amount of Cu^{2+} dopant in $CsPbCl_3$ can boost the PLQY of the NCs from 0.5% to 60% for the PL at 403 nm. Variations in the PLQY for PL at 430 nm (8–92%) and 460 nm (22–98%) were observed in $Cu:CsPb(Br/Cl)_3$. Thawarkar et al. [92] synthesized Ni-doped $CsPbBr_3$. $PbBr_2$, $NiBr_2$, and oleic acid were added to round-bottom flask and heated up to 200 °C, and previously prepared Cs-oleate was injected into the reaction mixture yielding Ni-doped CsPbBr3 NCs. They observed that Ni^{2+} doping of $CsPbBr_3$ leads to an increase in the PLQY without an observable shift in the PL peak position [92]. Similarly, Yong et al. [93] found that Ni^{2+} doping in $CsPbCl_3$ does not affect the PL energy but boosts the PLQY from 2.4% to 96.5%. However, the isovalent doping with Mn^{2+} and other metals led to enhanced PLQY due to improved passivation of the defect states associated with the halogen vacancies (V_X, X is Cl^-, Br^-, or I^-). These studies showed that the homovalent substitution at the B-site can alter the PL properties of the HPNCs in various ways, depending on composition, while retaining the original electronic structure relatively intact. This has important implications for exploitation of these materials in LED applications.

4.2 Heterovalent B-Site Ion Exchange

Bismuth (Bi^{3+}) is another suitable ion for the Pb^{2+} replacement in the ABX_3 PS structure. The Bi is located next to the Pb in the periodic table (group 5A) and the Bi^{3+} and Pb^{2+} have isoelectronic structures. Heterovalent doping presents an opportunity to modify the electronic structure of the perovskite via the B-site substitution. Since the Pb^{2+} and Bi^{3+} have similar ionic radii (Bi^{3+} 1.03 Å and Pb^{2+} 1.19 Å), the Bi^{2+} doping in ABX_3 perovskite does not significantly alter its tolerance factors. Zhou et al. [94] were the first to report doping of $MAPbI_3$ perovskite thin films with Bi^{3+}. The perovskite precursor solution was prepared by mixing MAI and PbI_2 in a 1:1 molar ratio in DMF and additional BiI_3 in DMF was added to the mixture to achieve desired Bi-doped $MAPbI_3$. Then the solution was spin coated on a glass substrate to form the Bi-doped $MAPbI_3$ thin film. They showed that with Bi^{3+} doping, the PL shifts from visible to NIR spectral range from 850 to 1600 nm. Abdelhady et al. [95] demonstrated that doping of Bi^{3+} in the single crystal (SC) $MAPbBr_3$ PS leads to a dramatic change

in its electric and optical properties. The heterovalent Bi^{3+} ions act as an electron donor and increase the electric conductivity (from $\sim 10^{-8}$ Ω^{-1} cm^{-1} for the undoped crystal to $\sim 10^{-4}$ Ω^{-1} cm^{-1} for the 10% Bi-doped $MAPbBr_3$ crystals). The Bi^{3+} doping increases the carrier densities and also converts the PS into p-type. They also observed that with increasing Bi^{3+} content the band edge of the doped crystal shifts towards lower energies. For example, for $MAPbBr_3$ with no doping the band edge is located at 570 nm and doping with $\sim$10% Bi^{3+} shifts the band edge to 680, which leads to change in the bandgap from 2.17 eV (for undoped $MAPbBr_3$) to 1.89 eV (for 10% Bi-doped $MAPbBr_3$). Later, spectroscopic ellipsometry measurements by Nayak et al. [96] in Bi^{3+}-doped $MAPbBr_3$ showed that bandgap energy decreases from 2.18 to 1.95 eV and that the red shift seen in the absorption spectra is due to the increase in the Urbach energy (from 19 meV to 50–55 meV), not due to the shift in the conduction band or valance band edge positions. This increase in the Urbach energy is related to the increase in the structural disorder, which directly affects the absorption onset of the Bi^{3+}-doped perovskites. Lozhkina et al. [97] observed similar effect in Bi^{3+}-doped $CsPbBr_3$ single crystals. Pristine and Bi^{3+}-doped $CsPbBr_3$ single crystals were grown using antisolvent vapor-assisted crystallization method. In a typical procedure, CsBr, $PbBr_2$, and $BiBr_3$ were dissolved in DMSO in various rations then transferred to another container, covered with cellulose membrane, and placed into a vessel with 20% ethanol solution as antisolvent. Solution was kept for 48 h at 40 °C to form the Bi-doped $CsPbBr_3$ single crystals. Though Bi^{3+} doping in $CsPbBr_3$ single crystal leads to a significant redshift in the absorption spectra, low temperature PL studies indicate that the excitonic peak position does not change, suggesting that the bandgap of the PS remains unaltered. Begum et al. [98] observed that Bi^{3+} doping in $CsPbBr_3$ HPNCs shows a small blue shift in the bandgap value (from 2.43 to 2.398 eV) along with a change in excited state carrier relaxation dynamics in $CsPbBr_3$ by reducing radiative transitions. Zhang et al. [99] reported substitution of Pb^{2+} ions in $CsPbBr_3$ HPNCs with Sb^{3+}. In this process, CsBr and $PbBr_2$ were dissolved in DMF with oleic acid and oleylamine. In another vessel, various stoichiometric amounts of $SbBr_3$ were dissolved in toluene, then the DMF solution containing perovskite precursor was added to the toluene, resulting in the formation of Sb-doped $CsPbBr_3$. While Sb^{3+} doping of $CsPbBr_3$ QDs in the 2.2–2.9 nm size had no impact on the bandgap, the PLQY was found to increase upon substitution. Liu et al. [100] synthesized Al-doped $CsPbBr_3$ via the hot-injection method. $AlBr_3$, $PbBr_2$, oleic acid, and oleylamine are taken on 1-ODE. Then, the temperature was raised to 150 °C and already prepared Cs-oleate solution was injected into the reaction mixture, resulting in formation of Al-doped $CsPbBr_3$. As a result of doping, a blue shift in the PL energy was observed. The above results indicate that while the effect of heterovalent B-site doping on the bulk $APbX_3$ PSs is relatively well understood, the understanding is less clear for the single crystal and HPNC systems. The effects of doping on the properties of HPNCs are summarized in Fig. 12.
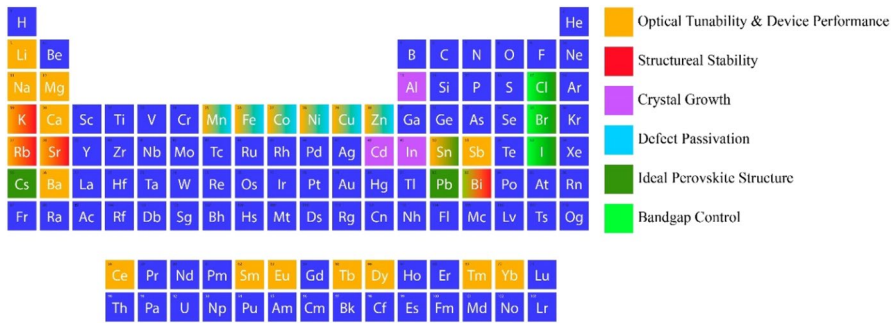
**Fig. 12** Overview of the effects of doping on the properties of HPNCs

5 Postsynthesis Phase Modification

In addition to composition, the phase and optical properties of the HPs can also be controlled by various postsynthesis modifications. These include surface modification/functionalization of the perovskite NCs via ligands exchange and specific interactions, irradiation by light, application of external pressure, water-assisted phase control strategies, etc.

5.1 Transformations via Chemical Treatment

Postsynthesis surface treatment by ligands is very useful for tuning the optical properties of the HPNCs. The ligand exchange or addition of new ligands can lead not only to improvement in the optical properties but also to changes in the phase and/or the shape of the HPNCs. For example, 3D ABX_3 PS can be transformed into 2D AB_2X_5 PS via appropriate postsynthesis chemical treatment. In 2017, Balakrishna et al. [101] reported preparation of 2D $CsPb_2Br_5$ nanosheets via an addition/treatment of 3D $CsPbBr_3$ NCs with dodecyl dimethylammonium bromide (DDAB) spontaneously at room temperature. The transformation was experimentally monitored by electronic absorption spectroscopy. Within 10 min after addition of the DDAB, the authors observed a drop in the absorbance in the 400–520 nm region and an increase in the absorbance at 320 nm. The increase in the absorbance at 320 nm was attributed to the formation of a $[PbBr_3^-]$ complex resulting from the exfoliation of the Cs^+ ions from the $CsPbBr_3$ by DDAB. Subsequently, emergence of another absorbance peak at 345 nm was observed. This was attributed to the formation of the $[Pb_2Br_5^-]$ complex, which gradually transforms into $CsPb_2Br_5$ nanosheets. During the transformation, the PL spectra showed a blue shift and the PLQY decreased from 70% to 4%. Another example of the post synthesis phase transformation is the conversion of bulk (3D) $CsPbBr_3$ HPNCs into zero-dimensional (0D) Cs_4PbBr_6 [102–104]. In this transformation, the externally added amines extracted the $PbBr_2$ from the $CsPbBr_3$ NCs, leading to the formation of the Cs_4PbBr_6. Palazon et al. [102] showed that addition

of tetramethyl-ethylenediamine (TMEDA) to orthorhombic $CsPbBr_3$ 8-nm nano-cubes in toluene at room temperature transforms them into 50-nm rhombohedral shaped Cs_4PbBr_6 in 2 min. During the transformation, the absorption peak shifted from 490 to 317 nm, with a complete loss of PL. Liu et al.[104] demonstrated that when alkyl thiol ligands are added to the $CsPbBr_3$ NCs hexanes or toluene solution, the 3D-$CsPbBr_3$ PS are transformed into 0D-Cs_4PbBr_6 NCs (Fig. 13). Interestingly, the transformation was found to be reversible. Chemical reactions of Cs_4PbBr_6 with organic acids [103], $PbBr_2$ [45] and Prussian blue [105] in hexane room temperature, were found to leads to the formation of 3D $CsPbBr_3$. It was also found that not only amines but also heat [105, 106], water [107] and pressure [108] can be used to accomplish this type of phase transformation. This also applies to hybrid perovskites. Recently, Huisman et al. [109] showed that thermal annealing of 0D-$MA_4Pb(Br_{1-x}I_x)_6 \cdot 2H_2O$ in air at ~75 °C triggers a dramatic transformation of the 0D phase to the 3D $MAPbI_{1-x}Br_x$ PS. They also demonstrated that this transformation can be reversed by simply cooling down the compound in air. The absorbance spectra revealed two sharp absorption peaks at 288 nm and 364 nm, which were attributed to the formation of $MA_4Pb(Br_{1-x}I_x)_6 \cdot 2H_2O$. Upon heating the compound to ~70–100 °C, an onset in the absorption spectra was observed at 800 nm, attributed to the formation of $MAPbI_3$ NCs.
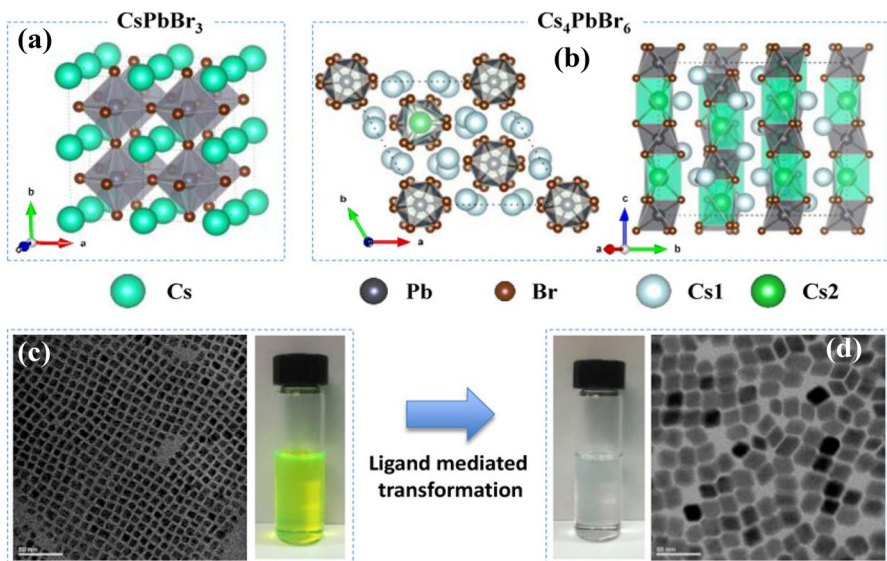
Fig. 13 Schematic crystal structure of **a** 3D-$CsPbBr_3$ and **b** 0D Cs_4PbBr_6. **c** TEM image of $CsPbBr_3$ NCs along with the digital image of the $CsPbBr_3$ after phase transformation. **d** TEM image of Cs_4PbBr_6 NCs along with the digital image of the Cs_4PbBr_6 after phase transformation. The chemical equation shows the reaction pathway for the 3D to 0D perovskite phase transformation. Reproduced with permission from ref. [104]. Copyright 2017 American Chemical Society

5.2 Transformations Induced by Irradiation

The postsynthesis phase transformation of PSs by chemical routes has been the most studied process for control of the PS phases. However, the number of studies of HPSs revealed that irradiation by visible/UV light can also lead to their postsynthesis phase and composition transformation. Photo-activated phase changes were previously studied in the CdSe quantum dots [110]. More recently, it was found that in the case of $APbBr_{1-x}I_x$, PS thin films, the irradiation by 400 nm pulsed laser light leads to a halogen phase separation with formation of "I"-rich and "Br"-rich domains [111]. The formation of the domains is associated with narrowing of the band gap in the domains with increased iodine content and widening of the bandgap in the domains with higher bromine content. In the case of single halide perovskite thin films in ambient atmosphere, the 532 nm laser light irradiation of the surface was found to lead to a phase degradation [112] or alteration [113]. Due to the large surface to volume ratio, NCs are much more sensitive to light exposure than their bulk counterparts. Several reports showed that a thin films of few-monolayer thick $CsPbBr_3$ nanoplatelets can be transformed from 2D to 3D materials when irradiated with 325 nm continuous-wave (CW) laser radiation of 20 mW cm^{-2} [114]. This process is generally referred to as the photo-induced phase transformation process (PDPT). From the mechanistic standpoint, the PDPT can be divided into two steps. In the first step, the surface ligands desorb from the NC surface, thanks to their relatively small binding energy [36]. In the second step, the ions diffuse between the nanoplatelets, which coalesce into larger structures (Fig. 14). The phenomenon was first observed by Wang et al. [114], followed by a report by Shamsi et al. [59]. The authors of these reports concluded that this kind of PDPT is not possible for hybrid PSs systems. Ha et al. [115] later contradicted this conclusion by observing transition from $n=2$ to $n=3$ layers in the $MAPbBr_3$ upon irradiation with 365 nm LED. Later, Roy et al. [116] showed that full conversion of quasi 2D $MAPbBr_3$ halide perovskite nanoplatelets (HPNPLs) to 3D $MAPbBr_3$ HPNPLs is possible by excitation of a 340 nm UV light source (12 mW) in hexanes. Similar transformations were also observed in HPNRs. In 2022 Sen et al. [117] showed UV-assisted (365 nm UV excitation) conversion of 2D Ruddlesden–Popper $MAPbI_3$ HPNPLs into stable 3D $MAPbI_3$ nanorods. Since understanding of PDPTs is essential for development of HP optoelectronic applications, more studies are needed to fully understand this phenomenon.

6 Size and Shape Control

The ability to effectively control the size and shape of the HPNCs is an important pre-requirement for their effective practical exploitation. Therefore, significant efforts have been devoted to the development of various strategies for synthesizing size- and shape-controlled hybrid or inorganic HPNCs. In the most commonly used synthetic approaches, the HPNCs are prepared as nanocubes. The cubic $CsPbBr_3$ HPNCs were first synthesized via the hot-injection method [44], where lead halide precursors were dissolved in the 1-ODE, organic amine, and an acid. Cs-oleate was
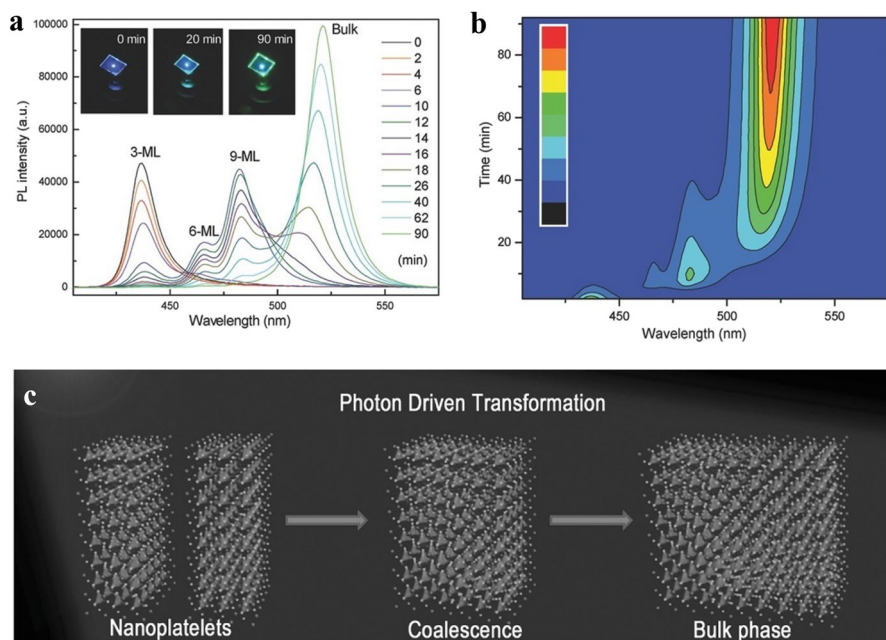
Fig. 14 **a** Time evolution of PL spectra of few layers thick CsPbBr$_3$ nanoplatelet. **b** PL variation mapping of few layers thick CsPbBr$_3$ nanoplatelet throughout the whole transformation process. The inset shows the PL photographs of the sample with varied exposure time. **c** Schematic illustration of PDPT; CsPbBr$_3$ nanoplatelets gradually coalesce and convert to 3D or bulk phase CsPbBr$_3$ under continuous photon irradiation. Reproduced with permission from ref. [114]. Copyright 2017 Wiley

injected at 140–180 °C, and the reaction was quenched using an ice bath. Depending on the injection temperature, the size of the nanocubes could be controlled in the range of 4–15 nm. Interestingly, the injection of Cs-oleate at a lower temperature (~130 °C) was shown to lead to the formation of halide perovskite nanoplatelets (HPNPLs) [118]. It was also observed that extended heating leads to formation of HP nanowires as a side product [119]. Almeida et al. [120] have shown that the size of the nanocubes can be controlled by systematic variations in the ratio of the oleic acid (OA) and oleylamine (OAm). The nanocubes in the size range from 4 to 16.4 nm were prepared by changing the OA/OAm ratio in the range 1:1 to 1:10. Protesescu et al. [47] synthesized FAPbBr$_3$ nanocubes by the hot-injection method, where presynthesized oleylammonium bromide (OAmBr) (halide source) was injected at 130℃ into the dissolved FA$^+$ and Pb^{2+} acetate precursor. This is slightly different from the conventional hot-injection method where PbBr$_2$ acts as a both Pb^{2+} and Br$^-$ source. By adjusting the amount of OAmBr, the size of the nanocubes was tuned from 5 to 50 nm.

Pan et al. [121] have varied the composition of carboxylic acids and amines to systematically investigate the effect of the acid and amine on the size and shape of the HPNCs. The results are schematically summarized in Fig. 15. The results show that an equal amount of amine and acid leads to a formation of monodisperse HPNCs. They also showed that by changing the Cs-oleate injection temperature
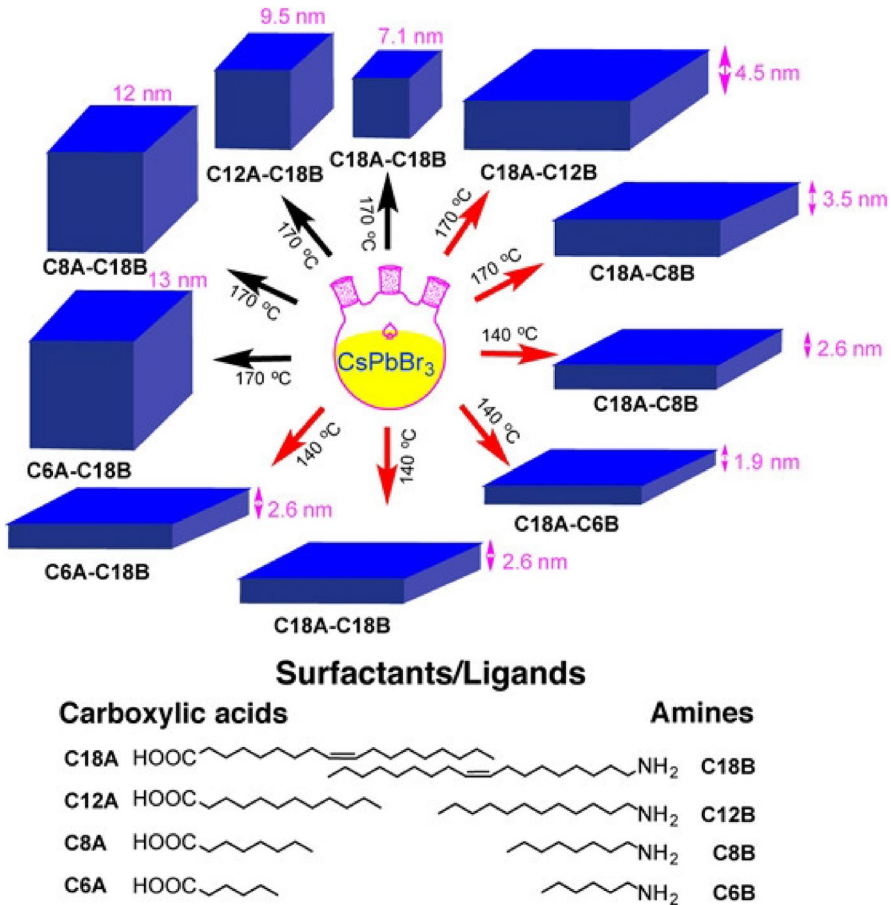
Fig. 15 Size and shape control approach during the hot-injection method. High reaction temperature with shorter carboxylic acid results in larger size nano cubes and shorter chain length amines result in thinner $CsPbBr_3$ nanoplatelets. Lower reaction temperature with shorter carboxylic acid results in nanoplatelets and shorter, long chain length amines result in thinner, and thicker $CsPbBr_3$ nanoplatelets, respectively. Reproduced with permission from ref. [121]. Copyright 2017 American Chemical Society

(140–200 °C) size of the $CsPbBr_3$ PNCs can be accurately controlled in the range 5–12 nm [44]. The initial efforts to prepare the layered HPNCs have focused on replacing small size organic cation with a long chain hydrocarbon cations. In the resulting structure the lead halide inorganic octahedral layers are spatially separated by the organic molecules. The chemical formula for this type of compound can be written as $L_2[ABX_3]_{n-1}BX_4$, where $n = 1,2,3,4,5,\dots \infty$ is the number of the octahedral layer. For example, for $n = 1$, the structure becomes L_2BX_4, which is a fully 2D PS structure. On the other hand, for $n = \infty$, the structure becomes ABX_3, which is a 3D structure. For $n = 2$ to few-layers-thick PSs are formed, known as the quasi-2D perovskites [116]. The optical properties of the layered PSs are primarily determined by the composition and thickness of the inorganic layer. The PSs with

different thicknesses of the inorganic layer exhibit different optical properties, due to the confinement effects similar to those observed for 3D perovskites. Compared with the 3D PSs, the layered HPNCs show higher structural stability due to the more negative enthalpy of formation. Around 2015, various research groups synthesized the first colloidal PS NPLs [71, 118, 122]. Initially, perovskite NPLs were identified as a by-product of the synthesis of the 3D perovskite NCs via the hot-injection method, particularly for the cases where injection was done at relatively lower temperatures (< 120 °C) [118]. Multiple efforts were also made to prepare NPLs by the LARP method. In the LARP method, perovskite precursors are first dissolved in a polar solvent such as DMF or DMSO and subsequently transferred to a nonpolar solvent for crystallization. Sichert et al. [71] were the first to report the preparation of MAPbBr$_3$ NPLs via the LARP method. In the reported procedure, they dissolved MABr, PbBr$_2$ and oleylammonium bromide (OAmBr) in DMF and transferred the solution into toluene for crystallization. By varying the MAX to OAmBr ratio, they were able to produce MAPbBr$_3$ NPLs with various numbers of inorganic layers. Subsequently, Akerman et al. [123] reported the synthesis of CsPbBr$_3$ NPLs ($n = 3$–5) via the LARP method. Berkenstine et al. [118] showed that injection of Cs-precursor into lead halide solution at relatively low temperatures (~120 °C) leads to a formation of HPNPLs. Depending on the injection temperature, they were able to synthesize CsPbBr$_3$ NPLs with $n = 1$–5. Vybornyi et al. [50] reported preparation of MAPbBr$_3$ NPLs via the hot-injection method, whereby the MA$^+$ precursor was injected at very low temperature (60 °C). Interestingly, it was observed that PS NPLs synthesized via the hot-injection method had a smaller lateral dimension (10–100 nm) [50, 118, 124] compared with the NPLs synthesized via LARP method (100–1000 nm) [71, 125, 126]. Shamsi et al. [127] showed that by adjusting the ratio of short and long ligands, lateral size of the HPNPLs can be systematically adjusted. The optical properties of HPNPLs possess some unique features. They are characterized by strong optical quantum confinement as well as dielectric confinement. HPNCs have an exciton Bohr radius of ~3 nm or larger, depending on the halogen [44, 71, 123, 128]. Since a single layer of PbX$_6$ octahedra is ~6 Å thick [116], even few layers thick HPNPLs are spatially confined along the axis perpendicular to the NPL layers. Moreover, due to the long chain amines, these structures are also dielectrically confined, which leads to large exciton binding energies with values up to several hundred meV [129–131] (Table 2).

In addition to NPLs, significant effort has been dedicated to synthesizing perovskite nanowires (NWs). In 2015, Zhang et al. [119] reported the first synthesis CsPbBr$_3$ and CsPbI$_3$ NWs via the hot-injection method. In this process, PbX$_2$ along with organic ligands were dissolved in 1-ODE and heated up to 150 °C. After the injection of previously prepared Cs-oleate into PbBr$_2$ solution, within $t < 10$ min, formation of nanocubes (NCs) with size ranging from 3 to 7 nm was observed by TEM. As reaction time increased to 10 min, a few thin NWs (9 nm in diameter) were found and with increasing time (40 min), reaction products were fully converted to HPNWs. Specifically, it was shown that by extending the reaction time after the injection of Cs-oleate, the lead and halogen source transform the HPNCs to HPNWs. Later, Tong et al. [132] synthesized various halide perovskite composition NWs by ultrasonication method. They found that during the sonication, initially

Table 2 Summary of the morphology and optical properties of nanostructures obtained from different acid–base combinations [121]

Sample	Temp (°)	Morphology	Size (nm)	PLQY%
C18A−C18B	170	Nanocube	7.1 ± 0.8	87
C18A−C18B	140	Nanoplatelet	2.6 ± 0.3	86
C12A−C18B	170	Nanocube	9.5 ± 1.2	63
C8A−C18B	170	Nanocube	12 ± 1.8	55
C6A−C18B	170	Nanocube	13 ± 2.3	59
C6A−C18B	140	Nanoplatelet	2.6 ± 0.4	38
C2A−C18B	120	Nanoplatelet	Not determined	22
C18A−C12B	170	Nanoplatelet	4.5 ± 0.6	51
C18A−C8B	170	Nanoplatelet	3.5 ± 0.4	61
C18A−C8B	140	Nanoplatelet	2.6 ± 0.3	46
C18A−C6B	140	Nanoplatelet	1.8 ± 0.3	36

cubic HPNCs are formed. They took Cs_2CO_3 and PbX_2 in 1-ODE with 1:1 volume ratio of oleic acid and oleylamine, and then, the reaction mixture was subjected to tip sonication at a power of 30 W for 10 min, which led to the initial formation of HPNCs. However, prolonged ultrasonication (up to 60 min) under similar reaction conditions lead to the formation of HPNWs. One of the challenges in the preparation of HPNWs is that they are typically prepared in a mixture with cubic 3D NCs. More recently, Zhang et al. [133] developed a new purification method, which increases the yield of HPNWs by using ethyl acetate (EA) as the antisolvent. This approach allows more effective separation of the ultrathin HPNWs from 3D NCs and other impurities.

7 Defects in HPNCs

In the cubic PS crystal structure, the "A" cation is in a 12-fold coordination, surrounded by four BX_6 octahedra. While this represents an ideal, equilibrium arrangement, real crystals often contain defect sites (e.g., at the surface and grain boundaries) where the structure deviates from this ideal arrangement. The types of defect found in the PS crystals depend on the details of the synthesis, such as precursor stoichiometry, methodology (LARP or hot-injection) and temperature (in bulk as well in the case of NCs) [20]. In addition, the irradiation with light, exposure to heat, moisture, and oxygen can also lead to formation of defect states and degradation or decomposition of the PS structure [134, 135]. Although PSs have unusually high defect tolerance in terms of optical and charge transport properties, detailed understanding of the defect formation and effects on the PS properties is critical for development of PS-based devices and applications. In general, the probabilities of the formation of various defects are related to their formation energies. Some information about these energies can be obtained from theoretical calculations, which then can provide guidance for the optimization of experimental preparation conditions [20, 136].

One of the characteristic features of HPS are low excitonic binding energies (E_b) (20 meV to 80 meV for the MAPbX$_3$ (X = I and Br) at room temperature. While a small E_b is an advantage for some applications, such as photovoltaics, they are less desirable in other optoelectronic applications, such as light emitting devices, where effective radiative recombination of carriers is desirable [137]. One way this problem can be addressed is by exploring the reduced dimensionality effects, as the E_b typically increases in quantum confined NCs. However, a significant reduction in the structure size also means significant increase in the surface-to-volume ratio, which typically translates into high probability of defects formation. Finding the optimal balance requires a thorough understanding of the parameters affecting the formation of defects in HPSs.

The defects typically observed in a semiconductor can be divided into two categories: (1) crystallographic defects, i.e., interruption in the perfect lattice of the semiconductor and (2) impurities, i.e., presence of a foreign element/ion within the semiconductor lattice. The defects can form as point defects (missing of an atom at a specific crystal position) or site substitution (atoms occupying the wrong position in the lattice) [138]. The probability of the internal defect formation varies with growth conditions and depends on the choice of solvent, precursor, temperature, and dopant [139]. In the case of ABX$_3$ PSs, the most commonly studied defect is the point defect. There have been 12 types of point defects reported in MAPbI$_3$ PSs. They are typically categorized into three vacancy-induced defects: V_{MA}, V_{Pb}, and V_I; three interstitial addition defects: MA$_i$, Pb$_i$, and V_i; and six antisite occupation defects: MA$_{Pb}$, MA$_I$, Pb$_{MA}$, Pb$_I$, I$_{MA}$, and I$_{Pb}$ [20, 136, 140–144]. Various theoretical studies have established that in PSs point defects have higher formation energies and contribute to formation of deep-level defect states, whereas point defects have lower formation energies and contribute to formation of shallow-defect states. It was also found that point defects, which contribute to formation of deep level defect states, do not produce nonradiative recombination centers [20, 142, 144]. Theoretical calculations also showed that I_{Pb}, I_{MA}, Pb$_i$, Pb$_I$, V_i, and Pb$_{MA}$ contribute mainly to the formation of deep level defect states; however, the understanding here is still evolving [145]. It was also observed that depending upon the formulation of the perovskite structure, the formation energy of Pb$_I$, V_I, and I_{MA} could be sufficiently low so as to lead to creation of nonradiative recombination centers. The shallow point defects can be classified into two categories: (1) acceptor defects (V_{MA}, V_{Pb}, I_i, MA$_{Pb}$, I_{MA}, and I_{Pb}) and (2) donor defects (V_I, MA$_i$, Pb$_i$, Pb$_{MA}$, MA$_I$, and Pb$_I$), which can be viewed as an unintentional doping in perovskite structure. Hence, by controlling the formation of defects in the PS structure, it is possible to prepare n-type or p-type materials. In the typical PS nanomaterial synthesis, depending on the synthesis method, various types of defects can be generated [146].

7.1 X-Site Defects

In 2015, Protesescu et al. [44] synthesized high quality HPNCs and observed that CsPb(I/Br)$_3$ NCs had significantly higher PLQY (~90–95%) than CsPb(Br/Cl)$_3$ NCs (~10–25%). Similar observation was made for the hybrid MAPbBr$_{3-x}$Cl$_x$

HPNCs listed in Table 3 [147]. In the Br–Cl perovskites, deep level trap states formed due to the formation of Cl^- vacancies (V_{Cl}). These deep-level traps act as nonradiative relaxation centers, contributing to reduction in the PLQY [148]. The formation of the vacancies can also be observed in the absorption spectra of the HPNCs. Urbach energy of the I–Br series is significantly higher than the Br–Cl series as a result of the higher level of disorder and density of defect states, leading to an increase in the probability of sub-bandgap transitions. Number of researchers explored various techniques to overcome this problem. Zhang et al. [33] synthesized the hybrid HPNCs via LARP method where the use of polar solvent is essential for formation of NCs. A strong interaction between the PbI_2 and the coordinating solvent (DMF/DMSO) led to formation of $PbI_2 \cdot$DMF/DMSO intermediates, which promote formation of the I vacancies (V_I). Under the ambient conditions, these vacancies are filled by oxygen molecules, which react to form PbO as an initial step in a gradual chemical degradation of the HPNCs [41]. In contrast, the HPNCs prepared by the hot-injection two-in-one precursor method (i.e., PbX_2, where X is Cl^-, Br^-, or I^- is the source of lead and halogen simultaneously) typically suffer from halogen deficiency, which leads to the formation of halogen vacancies. These halogen vacancy defect states increase the efficiency of the nonradiative relaxation and lower the PLQY of the HPNCs [44, 55]. Dutta et al. [149] demonstrated that annealing of HPNCs with long-chain ammonium halides at higher reaction temperatures (250 °C) reduces the formation of defect states and increases the PLQY to~50%. To minimize the halogen defects, halogen-rich conditions are often used in the synthesis of HPNCs. Liu et al. [55] developed a three-precursor method to achieve halogen-rich conditions, for example by replacing PbX_2 with PbO and NH_4X. As shown in Fig. 16, this approach leads to high PLQY in the HPNCs [55]. NH_4X provides excess halogen during the reaction which reduces the halogen vacancy and hence increases the PLQY of the HPNCs. This kind of understanding of halogen defects and their effect in the optical properties is essential for development of effective device applications.

Table 3 Variation of the optical properties with systematic change in the halogen composition

| $MAPbBr_{3-x}Cl_x$	PL Peak (nm)	FWHM of PL spectra (nm)	τ_{ave} (ns)	PLQY (%)
$x=1$	520	20	97.4	73
$x=0.6$	505	22	64.69	65
$x=1.2$	470	22	32.20	35
$x=1.8$	436	20	21.94	24
$x=2.4$	416	20	21.39	12
$x=3.0$	399	17	14.54	8

With increase in Cl concentration, PLQY decreases, which clearly indicates the formation of VCl in the perovskite structure [147]
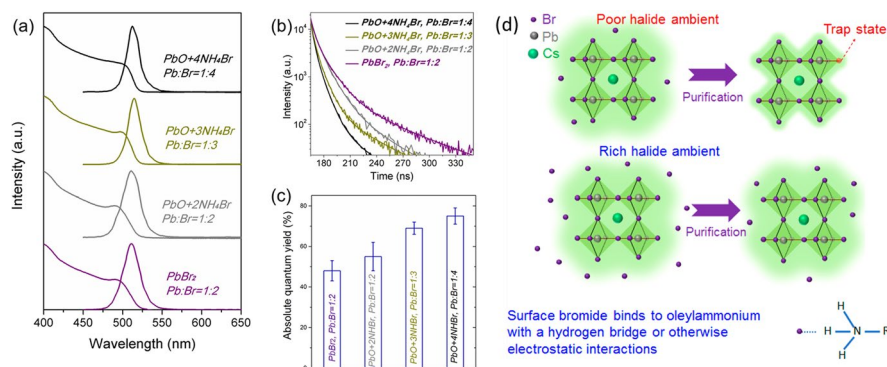
Fig. 16 a Steady-state UV and PL spectra of perovskite NCs synthesized via the three-precursor method. **b** Time-resolved PL decay and respective curve-fitting for CsPbBr$_3$ NCs. **c** Average PLQY values of various perovskite NCs synthesized in different halide circumstances. **d** Schematic diagram of the effect of rich/poor halide conditions on the optical properties of perovskite NCs. Reproduced with permission from ref. [55]. Copyright 2017 American Chemical Society

7.2 B-Site Defects

Various reports demonstrated that partial substitution/doping of the B-site of the perovskite can reduce point defects, structural disorder or distortion in the perovskite octahedra. It was also observed that the PLQY of pristine CsPbCl$_3$ can be significantly enhanced by the postsynthesis treatment with CuCl$_2$, suggesting that this treatment reduces the Cl$^-$ vacancies [150]. In one example, Yong et al. [93] showed that doping of CsPbBr$_3$ perovskite NCs with Ni^{2+} significantly reduces the halogen defects (V_X) and increases the lattice order of the PS structure, which leads to enhanced exciton radiative recombination. Specifically, 2–3% substitution of Pb^{2+} with Ni^{2+} led to increase of PLQY from ~1.2 to ~93% (see Fig. 17a, b) [93]. Similarly, doping with Zn^{2+} ions was also found to lead to defect passivation in CsPbBr$_3$ perovskite NCs and a significant increase in the PLQY from 54% to 74% (see Fig. 17c, d) [151]. The defect passivation by Zn^{2+} was attributed to the ability of the ZnBr$_2$ to produce Br-rich conditions in the PS by filling the halogen vacancies. Mondal et al. [152] showed that postsynthesis doping of Cd^{2+} into CsPbCl$_3$ NCs leads to formation of NCs with PLQY near unity (96 ± 2%). The defect passivation by the CdCl$_2$ post-treatment was investigated by time-resolved photoluminescence (TRPL) and ultrafast transient absorption spectroscopy (TAS) at various temperatures [152]. The results showed that the suppression of the nonradiative transition in the doped CsPbCl$_3$ NCs can be attributed to the passivation of the defect states associated with the V_X vacancies. The conclusions of the study are schematically summarized in Fig. 17e. In other studies, it was shown that doping of the B-site in the PS structures can also lead to formation of new defect states. For example, doping of MAPbI$_3$ single crystals by Bi^{3+} was found to enhance the electrical conductivity of the material by factor of three [153]. Increase in the measured Urbach energy together with a significant blue shift in the PL spectra were attributed to the
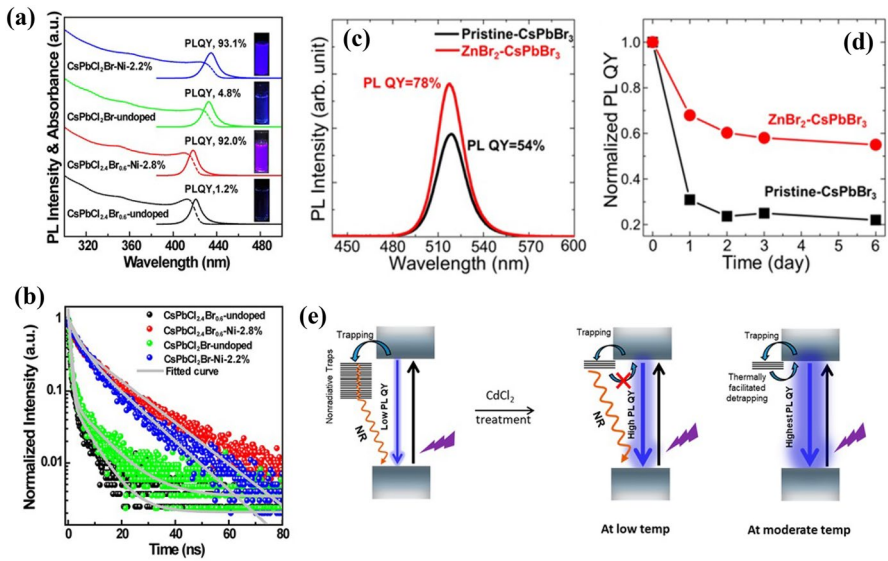
Fig. 17 a UV–visible light and PL spectra of undoped and Ni-doped CsPb(Cl/Br)$_3$ NCs showing the change in the PLQY of the HPNCs. **b** PL decay spectra of undoped and Ni-doped CsPb(Cl/Br)$_3$ NCs. Reproduced with permission from ref. [93]. Copyright 2018 American Chemical Society. **c** Emission spectra and PLQYs of pristine and Zn-doped CsPbBr$_3$ NCs. **d** PLQY of CsPbBr$_3$ NPs after exposure to ambient atmosphere as a function of time. Reproduced with permission from Ref. [151]. Copyright 2017 American Chemical Society. **e** Schematic depiction of the effect of Cd^{2+} doping on the exciton relaxation in CsPbBr$_3$ NCs. (NR is a nonradiative recombination process). Reproduced with permission from ref. [152]. Copyright 2018 American Chemical Society

formation of Bi^{3+}-related donor states. These donor states release more electrons to the conduction band, which results in the observed increase in conductivity. First-principles modeling by Mosconi et al. [154] showed that the presence of the Bi^{3+} dopants in the MAPbI$_3$, induces formation of deep trap states. Similar observation was also made in the case of Bi^{3+}-doped MAPbBr$_3$. Abdelhady et al. [95] found that by doping MAPbBr$_3$ single crystals with Bi^{3+}, the conductivity of the crystals increased by four orders of magnitude. While pristine MAPbBr$_3$ is a p-type semiconductor, Hall effect measurements showed that after Bi^{3+} majority doping carriers switch from holes to electrons. The authors of the study also reported that Bi^{3+} doping reduces the bandgap by 300 meV. However, later Nayak et al. [96] showed that the appearance of a band gap shift can also be explained in terms of the increase in the Urbach energy associated with the Bi^{3+} doping. The doping of CsPbBr$_3$ PSNCs by Bi^{3+} was found to also lead to an overall increase in the amount of defects and a decrease in the PLQY from 78% to 8% [98]. In spite of the extraordinary success and progress, in the understanding of the effects of B-site doping on defects, there are many questions that remain unanswered as far as the effective passivation strategies or controlled generation of new defects in the HPSs.

7.3 A-Site Defects

In the PS family of materials, conduction band minimum (CBM) is mainly formed by the 6p orbitals of Pb^{2+}, with a minor contribution from 5s orbitals of I^-, 4s orbitals of Br^-, or the 3s orbitals of Cl^-, whereas the valence band maxima (VBM) are comprising mainly the 6p antibonding orbitals of Pb^{2+} and the 5s orbitals of I^-, 4s orbitals of Br^-, or the 3s orbitals of Cl^-. Theoretical modeling showed that there is no contribution from the orbitals of organic cations to the CBM and VBM [52]. This is schematically shown in Fig. 2. The analysis also shows that A-site cationic bonding states are located deep inside the VB and do not hybridize with PbI_6 octahedra near the VBM or the CBM. While the organic cations do not contribute to the formation of states near the VBM or CBM, they play a major role in providing structural stability of the PS materials [155]. Since the electronic contributions from the A-site cations lie deep inside the band structure, changing of the A-site cation does not directly influence the formation of defects. Rather, the substitution of the A-site affects the electronic structure and optical properties indirectly. For example, doping of $MAPbX_3$ (MA ionic radius 0.18 nm) with a larger cation such as FA^+ (ionic radius 0.22 nm) or smaller cation such as Cs^+ (ionic radius 0.167 nm) or Rb^+ (ionic radius 0.152 nm), increases (FA^+)/decreases (Cs^+, Rb^+) the $B-X$ bond length and causes the lattice expansion (FA^+)/contraction (Cs^+, Rb^+), leading a decrease(FA^+)/increase (Cs^+, Rb^+) in the bandgap energy [156].

8 Degradation of HPNCs

## 8.1 Oxygen and Moisture-Induced Degradation

Although, brief exposure of the PS films to water can enhance their thin film quality during the perovskite crystallization [157, 158], extended contact of PSs to an atmosphere with high relative humidity (RH) leads to their irreversible degradation. Leguy et al. [159] showed that when HPSs are exposed to water vapor, due to the hygroscopic nature of the MA^+ ion, a hydrated $MAPbI_3$ PS phase $(MAPbI_3 \cdot H_2O)$ is formed. This phase form can be fully reverted to $MAPbI_3$ perovskite (nonhydrated) upon drying [159]. Ahn et al. [160] showed that it is the charges trapped in the defect states located at the grain boundaries or surfaces that are primarily responsible for this reversible degradation. Though the excess amount of water eventually leads to complete degradation of the perovskite structure. In addition to water, molecular oxygen is another important source of degradation of HPSs. In 2015, Aristidou et al. [161] showed that when $MAPbI_3$ PS is exposed to O_2 in the presence of light, it decomposes rapidly into MA, PbI_2, and I_2. It was proposed that degradation process is initiated by a light induced conversion of O_2 into O_2^- super oxides, which react with MA^+ cations. The theoretical analysis showed that O_2^- likely forms by the reaction of the ambient O_2 with the negatively charged iodine in the (V_I) defect sites (Fig. 18). In the proposed mechanism, the V_I defects serve as traps for the atmospheric O_2, which upon photoexcitation and interaction with I^- turns into highly reactive superoxide, which gradually degrades the PS. This can be
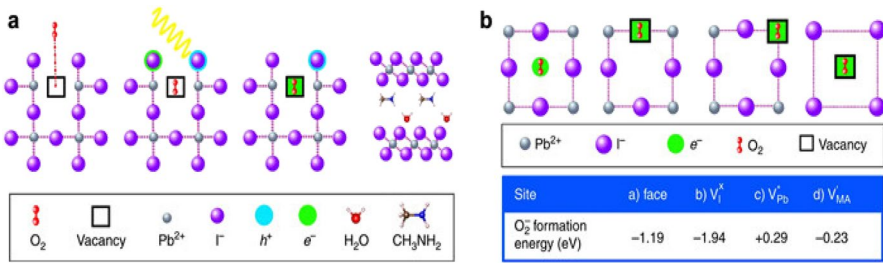
Fig. 18 **a** Schematic representation of the interaction of the O_2 with MAPbI$_3$ during the superoxide formation. **b** Binding and reduction of O_2 at various sites of MAPbI$_3$ along with the calculated superoxide formation energy of different sites. Reproduced with permission from ref. [161]. Copyright 2017 Nature

experimentally observed as gradual reduction in absorbance spectra in HPS exposed to dry air (including oxygen). In contrast, it was found that a controlled, short-term exposure of a HPS to moisture passivates the surface traps, which increases the observed PL. Consistently, with this assessment, Brenes et al. [162] showed that PL intensity of the HPSs depends not only on the PS morphology but also on the environment to which the HPS is exposed (see Fig. 19a–c) [162]. The authors also found that when exposed to O_2 and/or H_2O molecules the PL of the PS grains, which initially show weak PL, is significantly enhanced, while the grains, which are initially bright, remain relatively unaffected by the exposure to O_2 and/or H_2O. To understand these results, density functional theory calculations were performed. Consistent with the studies mentioned above, the analysis showed that O_2 binds strongly to the surface iodide vacancies. These oxygen molecules passivate the carrier trap states, which are generated from the iodine vacancies. This passivation of defect states by oxygen molecules not only enhances the emission properties of the perovskite but also increases the electric conductivity of the MAPbI$_3$. Huang et al. [163] observed similar effect in the CsPbBr$_3$ NCs. They reported that when CsPbBr$_3$ NCs thin films are exposed to relative humidity of 60–80% for 8 h, in the absence of O_2, no PL intensity decrease was observed. When the same films were exposed to the oxygen atmosphere, PL intensity increased because of the formation of superoxide with surface halogen vacancies. This phenomenon is known as the oxygen boost effect. However, oxygen boost effect can be seen only with short-time illuminations. Upon continuous illumination, the highly emissive green color HPNCs thin film turn into nonemissive, yellow-colored film. Mukherjee et al. [164] reported similar observation in studies of single crystals of MAPbBr$_3$ NPLs. They observed an initial increase in the PL intensity when MAPbBr$_3$ NPLs were exposed to O_2 atmosphere. Upon continuous exposure to O_2, the NPLs eventually lost the PL completely. They also observed two-state blinking pattern (with less emissivity) under inert conditions and photo-brightening blinking pattern (with more emissivity) in O_2 and moist air atmosphere. These observations indicate that under inert conditions HPNCs are stabilized but they lose the PL. On the other hand, in O_2 and moist air atmosphere the HPNCs are more emissive but have reduced stability. Stoeckel et al. [165] studied the electrical response of organohalide PSs in the presence of oxygen. They found
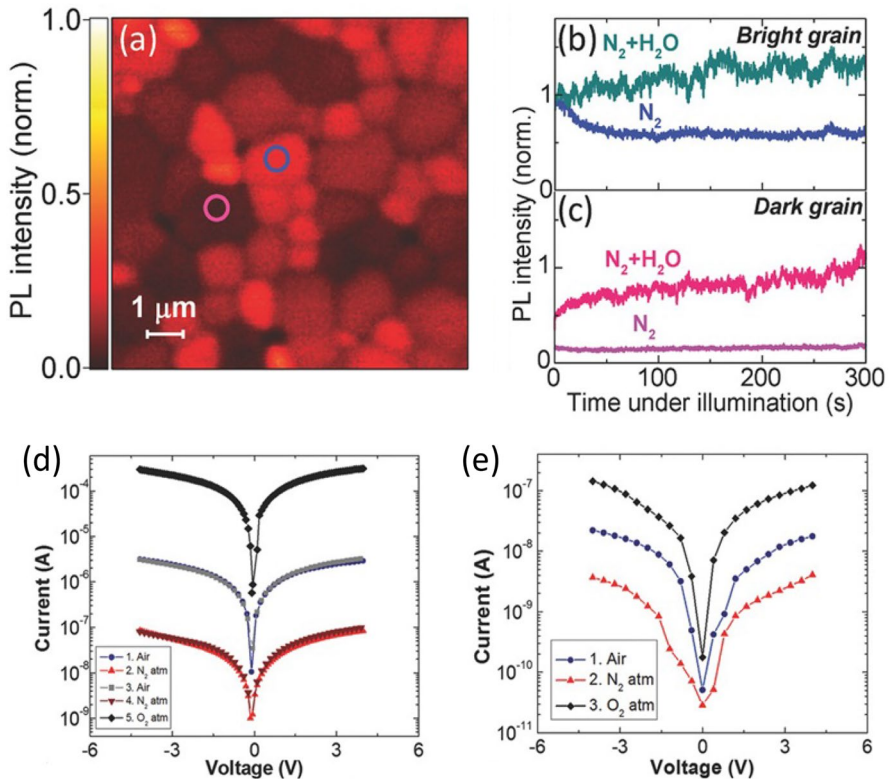
Fig. 19 **a** PL mapping of a MAPbI$_3$ perovskite film in dry nitrogen. **b** PL emission from a bright grain [blue circle in (**a**)] shows photo brightening under O$_2$ and H$_2$O along with a steady emission in inert atmosphere. **c** A dark grain [pink circle in (**a**)] under dry nitrogen shows steady emission and shows photo brightening under humid environment ($\approx$45% relative humidity). Reproduced with permission from ref. [162]. Copyright 2018 Wiley. Current–voltage measurement of (**d**) two-step deposited perovskite thin film (**e**) and single-step deposited perovskite thin film at different O$_2$ concentrations. Reproduced with permission from ref. [165]. Copyright 2017 Wiley

a 3000-fold increase in the electric conductivity when HPS films were exposed to the oxygen atmosphere (Fig. 19d, e). The studies discussed in this section show that oxygen and moisture can, on a short-term, passivate the defects at surfaces or the grain boundaries, but in the long term, they cause the degradation of the PSs. Better understanding of these processes is essential for development of high-performance HPS devices.

8.2 Light-Induced Degradation

Experimental studies have shown that hybrid/inorganic ABX$_3$ HPSs are very sensitive to light, particularly in the ultraviolet light spectral range, regardless of whether the material is in the bulk form or in the form of NC. With respect to phase and composition stability of HPSs, light can be viewed as a reagent. Numerous

examples consistent with this assessment can be found in literature. In one example, Merdasa et al. [166] showed that exposure of $MAPbI_3$ to 514-nm CW laser light leads to a large blue-shift (60 nm) of the PL spectrum with a sharp decrease in the PL intensity, indicating structural degradation of the PS to PbI_2 form. This was attributed to the light-induced migration of the MA ions, distorting the lattice structure of the PS and altering the Pb–I–Pb bond angle, which changed the bandgap and led to the formation of the PbI_2 phase. Similar effect was observed for $CsPbI_3$ HPNCs [167], by single crystal spectroscopy, which upon a visible light irradiation of 466 nm pulsed laser diode underwent an irreversible, photo-induced blue shift of the PL and ultimately to a complete PL quenching. They found that both light and water can independently degrade $CsPbI_3$ NCs. Light acts as a catalyst speeding up the degradation. Light induced effects resemble the vacancy-mediated A-site ion migration [168], as the photoexcitation reduces the barrier to ion migration. As a result of the ion migration, in a short-term, a capacitance builds up in the PS, which leads to an observation of hysteresis in the J–V characteristics of the HP solar cells [169, 170]. In the case of mixed halide PSs, a continuous irradiation of the mixed HPSs (thin film or NCs) leads to phase segregation due to ion migration [113]. Hoke et al. [171–173] were first to report on the ion migration behavior in the mixed HPSs. Halide ion migration produces in the mixed halide $MAPb(Br/I)_3$ PSs 'I' rich and "Br"-rich domains. The resulting phase segregation leads to formation of regions with a narrower bandgap in the case of iodine and wider bandgap in the case of bromine. A reversible red shift in the PL spectra is observed in the mixed halide perovskite thin films due to the halogen ion migration caused by photoinduction. The photoexcitation was also found to lead to generation of a lattice strain [174–176]. To minimize the irradiation generated lattice strain, ions migrate to reach an equilibrium position and a halogen rich domain are formed, which lead to the observed in the PL spectra. On the other hand, Zhang et al. [177] showed that $CsPbBr_{1.2}I_{1.8}$ NCs (on a single-particle level) undergo a nonreversible blue shift from 630 to 520 nm and then eventually lose the emission leads as they photodegrade. Although, the formation of halogen rich domains is a reversible process and the interruption of irradiation can restore the system to its original state, the photoinduced ion migration is an undesirable effect from the standpoint of development of optoelectronic applications. In addition, it was found that iodine-rich regions can act as nonradiative recombination centers, which can trap the photo-generated charge carriers and significantly reduce important photovoltaic parameters such as open-circuit voltage and quantum efficiency [174, 178].

9 Electrochemistry and Spectroelectrochemistry of HPNCs
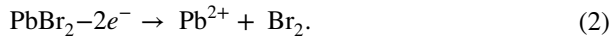
Charged HPNCs play an important role in technologies such as photovoltaics, light-emitting diodes, photodetectors, and others. These devices rely on efficient NC-to-NC hopping of carriers to or from electrodes. Significant populations of charged NCs can form during the device operation. Spectroelectrochemistry is a useful tool for studies of how perovskite NCs can be charged, how the charge migrates in HPNC structures and how charging affects their optical properties. In spite of its practical

importance, this understanding is so far limited. This is mainly due to the instability of the HPNCs upon charging. In 2016, Vikash et al. [179] used electrochemistry to investigate the absolute energy offsets of the conduction band minima (CBM) and valance band maxima (VBM) in the $CsPbX_3$ (X is Cl^-, Br^-, or I^-) NCs, while systematically varying the halogen composition. Cyclic voltammetry (CV) results showed that as the halogen was changed from $X = Cl^-$ to Br^- to I^-, the VBM systematically shifted from ~1.8 to ~1.4 V to ~1.0 V (versus NHE), whereas the CBM shifted from -1.3 to -1.2 V to -1.1 V, respectively. Samu et al. [180] investigated the charging of $CsPbBr_3$ and $MAPbI_3$ thin films by electrochemistry and spectroelectrochemistry, coupled with X-ray diffraction (XRD) and X-ray photoelectron (XPS) spectroscopies. In the case of $CsPbBr_3$, two oxidation peaks, one at ~0.8 V and one at ~1.5 V, and one reduction peak at ~ -1.0 V, with respect to NHE electrode, were observed. During the oxidation, the absorbance at 518 nm was observed to first increase at the first oxidation potential, primarily due to the changes in PS film scattering, and then gradually decrease again following the second oxidation (Fig. 20a–c). During the reduction cycle, the absorption decreased dramatically at the potentials more negative than -1.0 V (-1.2 V versus Ag/AgCl) (Fig. 20b). The observed changes were assigned to the chemical processes summarized in Eqs. 1−3 below:
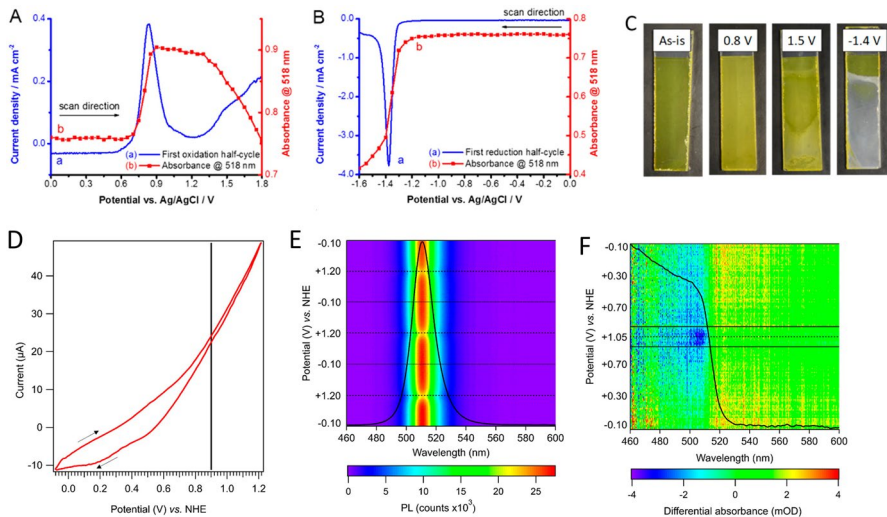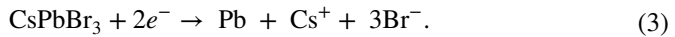

Fig. 20 Spectroelectrochemical data was recorded for $FTO/TiO_2/CsPbBr_3$ films during the **a** oxidation and **b** reduction half cycle together with the absorbance change at the excitonic peak. **c** Photographs of perovskite deposited electrodes after CV cycle. Reproduced with permission from ref. [180]. Copyright 2018 American Chemical Society. **d** CV of a $CsPbBr_3$ NC electrode. The estimated VB edge position is marked by the black line. **e** PL of a NC electrode as a function of the applied potential during three CV scans ranging from -0.10 to $+1.20$ V. Hole injection into the VB edge of the NCs, starting at $+0.9$ V, quenches the PL, which largely recovers when the applied potential is lowered to below $+0.9$ V. **f** Differential absorbance of a NC electrode as a function of the applied potential, ranging from -0.10 to $+1.05$ V. The initial absorption spectrum is plotted in black. Reproduced with permission from ref. [182]. Copyright 2021 American Chemical Society

Oxidation:

$$CsPbBr_3 - e^- \rightarrow PbBr_2 + Cs^+ + 0.5Br_2, \tag{1}$$

$$PbBr_2 - 2e^- \rightarrow Pb^{2+} + Br_2. \tag{2}$$

Reduction:

$$CsPbBr_3 + 2e^- \rightarrow Pb + Cs^+ + 3Br^-. \tag{3}$$
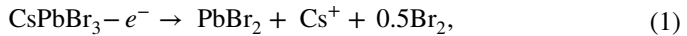
Similar observations and conclusions were reached by Lee et al. [181] in studies of $CsPbBr_3$ nanoparticulate thin films. The reasons for the observations can be understood by referring to the energy diagram shown in Fig. 21a. Because the oxidation reactions (1) and (2) are thermodynamically more favorable than the injection of a hole into the VB of the $CsPbBr_3$, the application of the potential required for injection of a hole leads to irreversible chemical changes in the composition of the material according to reactions (1) and (2). Similarly, on the reductive side, the thermodynamically favorable reaction (3) effectively competes with the electron injection into $CsPbBr_3$ CB. The oxidation of iodine and reduction of Pb^{2+} are thermodynamically even more favorable in the case of $CsPbI_3$. Therefore, application of potentials required for hole/electron into the VB/CB leads to even more rapid chemical degradation of the HPNCs. In contrast, $CsPbCl_3$ was shown to have significantly better stability with respect to chemical degradation under the conditions of electrochemical charging. More recently, Mulder et al. [182] showed that the reversible p-doping of $CsPbBr_3$ NCs can be achieved by modification of their surface properties by synthetic means. In the preparation of $CsPbBr_3$ NCs, instead of
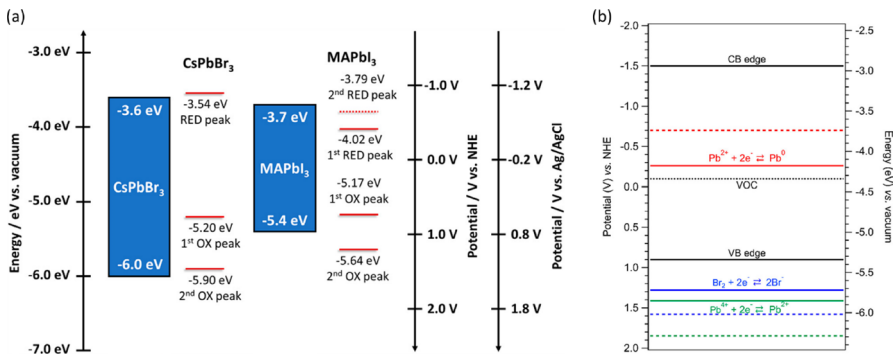
Fig. 21 **a** Comparison of the band edge positions and the potentials of various redox reactions observed in lead halide perovskites. Reproduced with permission from ref. [180]. Copyright 2021 American Chemical Society. **b** Energy diagram, indicating the energy level of the VB edge, CB edge, and V_{OC} of the measured $CsPbBr_3$ NCs. Reproduced with permission from ref. [182]. Reproduced with permission. Copyright 2018 American Chemical Society

$PbBr_2$, benzoyl bromide was used as the halide source. This led to the formation of halogen-rich $CsPbBr_3$ NCs, thermodynamically stabilized with respect to the electrochemical oxidation. In the stabilized HPNCs, the spectroelectrochemical studies (Fig. 20d–f) showed that observed changes in the emission and absorption are due to the reversible injection of hole into the core of the NCs. These results can be understood in terms of the energy diagram shown in Fig. 21b. The use of the halogen-rich precursor led to stabilization of the VBM (~0.9 V versus NHE). As a result, the competing oxidation processes, oxidation of Br^- and Pb^{2+} are thermodynamically less favorable. The injection of electron into the CB was not successful due to the rapid reduction of the HPNCs, according to reaction (3). These results show that surface modification can be used as an effective tool in modifying the electronic structure of HPNCs, which leads to their stabilization with respect to carrier doping.

In a separate study, Wong et al. [183] investigated electrochemiluminescence (ECL) of $CsPbCl_3$ and Mn-doped $CsPbCl_3$ in the presence of benzoyl peroxide as a coreactant. In the electrochemical studies of the undoped $CsPbCl_3$ two oxidation peaks were observed, one at 0.8 V and 1.2 V and one reduction peak at -1.7 V. The authors attributed these peaks to injection of first and second hole into the VB and injection of electron into the CB, respectively. When attempting to generate ECL using a rapid potential step past the potentials for hole or electron injection, no ECL was observed in the undoped $CsPbCl_3$. This suggests that the observed electrochemical response is likely dominated by the electrochemical degradation of the $CsPbCl_3$ NCs, similar to the processes shown in reactions (1)–(3), rather than hole or electron injection. A weak ECL was observed in Mn-doped $CsPbCl_3$ following the potential step past 0.7 V, attributed to partial stabilization of the charged HPNC by the Mn dopant [184].

10 Summary and Outlook

The advances summarized in previous sections clearly show that over the past decade HPNCs were established as a distinct new class of materials with unique properties and great practical potential. Diverse set of approaches for the preparation of HPNCs were elaborated, with the hot-injection method representing arguably the most important advance. Good progress was made in identifying the key parameters influencing the size and shape of the produced HPNCs. Development of approaches for effective doping of HPNCs opened path to additional tuning of their electronic structure and optical properties, further extending their utility. Important advances were made in understanding of the relationship between the composition, defects and optical properties of HPNCs, chemical processes responsible for their degradation, as well as the effects of charge injection. These advances represent the necessary early steps towards the development of stable materials suitable for exploitation in applications.

Despite, and in many instances thanks to this significant progress, important questions and challenges remain, or have emerged, that need to be answered before HPNCs will enjoy broad acceptance as materials of choice for optoelectronic, optical, electrical, chemical, medical, or other applications. One example is the

mechanism and the dynamics of the NC growth. While for chalcogenide NCs the dynamics of NC growth is reasonably well described by La Mer type diagrams with various distinct steps, this is not the case for HPNCs. Due to the ionic nature of the perovskite structure, in the hot-injection or LARP methods HPNCs are formed nearly instantaneously, which makes it difficult to resolve various stages of the crystal growth process (e.g., nucleation, growth, and ripening). Hence, for the HPNCs the general crystal growth kinetics and mechanism were not yet clearly established. For majority of reactions, the mechanism is specific for a single type of reaction or for a specific size or shape, with dimension tuning primarily achieved through thermodynamic control. Another area, where more advances are needed is the understanding of the HPNC surface chemistry. Due to the highly dynamic nature of HPNC surface ligands, the HPNCs are very sensitive to surface treatment and/ or change of environment. During purification, PLQY of HPNCs can be reduced by 20–40% due to removal/substitution of surface ligands, yet our understanding of the origins of the high lability of the surface ligands and potential solutions are quite limited. Previously proposed use of bidentate ligands may be a step in a right direction, but more systematic studies are needed in this area. Another challenge to be addressed is the long-term chemical stability of the HPNCs. Though it is observed that $CsPbBr_3$ NCs are relatively stable over a long period of time, preparation of $CsPbI_3$ NCs with stable phase and PLQY is quite challenging. Moreover, while significant progress was made in the synthesis of inorganic halide perovskite nanocubes, the examples of organic halide perovskite nanocubes are much more limited. Significant efforts were dedicated to development of methods for synthesis of perovskite NPLs, but our understanding of how to reproducibly grow HP NPLs with control over thickness and shape are limited. Additionally, the extent to which perovskite NPLs exist as isolated sheets in a colloidal solution rather than as small crystallites of the Ruddlesden–Popper phase remains unclear. Therefore, systematic studies of the behavior of HP NPLs in colloidal solutions are needed. Moreover, since the PLQY of these relatively low as compared with the cubic analogues, there is a need for studies aimed at improving the PLQY the perovskite NPLs.

To date, the hot-injection and LARP methods, the most utilized approaches for synthesis HPNCs, utilized long chain alkylamines to stabilize the NCs. These types of ligands represent an electronic energy barrier, hindering interparticle electronic coupling and thereby constraining the potential applications of the HPNCs in optoelectronics and electronics. To address this challenge, new synthetic or ligand-exchange approaches need to be developed that will allow preparation of HPNCs with more conductive or smaller ligands, without compromising the quality and stability of the HPNCs. An additional problem from the standpoint of electronic application of HPNCs is the ion migration, which leads to hysteresis in the device performance. New approaches need to be identified that will limit the negative impact of the ion migration on the performance of devices.

In the case of the doped perovskite structures, knowledge of the dopant location within the HPNCs is important from a fundamental as well as practical standpoint. However, currently we have limited information about whether the available doping approaches yield NCs with dopants located on the surface of the HPNC or inside its lattice. This is in part due to the low stability of HPNCs under the standard electron

microscopy conditions. Creative solutions to overcoming this problem are needed to better understand the structure of doped HPNCs. More studies are also needed to better understand the origins of the defects in HPNCs during the synthesis and as well as during the interaction with the ambient environment and their effect on optical and electrical properties of HPNCs. Presence of toxic lead in the structure of HPNCs remains a challenge from the standpoint of their potential commercial utility. While some advances were made in this area, the optical properties of prepared lead-free HPNCs are much less appealing than the lead-based counterparts. Thus, more effort is needed in development of lead-free HPNCs. The intrigue of these and similar questions and challenges guarantees that HPNCs will remain an intense area of research in the foreseeable future.

Declarations

Conflict of Interest On behalf of all authors, the corresponding author states that there is no conflict of interest.

References

1. Wells HL (1893) Z Anorg Chem 3:195. https://doi.org/10.1002/zaac.18930030124
2. Mitzi DB (1999) In: Karlin KD (ed) Progress in Inorganic Chemistry, Vol 48 p 1
3. Mitzi DB, Feild CA, Harrison WTA et al (1994) Nature 369:467. https://doi.org/10.1038/369467a0
4. Mitzi DB, Wang S, Feild CA et al (1995) Science 267:1473. https://doi.org/10.1126/science.267.5203.1473
5. Kojima A, Teshima K, Shirai Y et al (2009) J Am Chem Soc 131:6050. https://doi.org/10.1021/ja809598r
6. Kim H-S, Lee C-R, Im J-H et al (2012) Sci Rep 2:591. https://doi.org/10.1038/srep00591
7. Lee MM, Teuscher J, Miyasaka T et al (2012) Science 338:643. https://doi.org/10.1126/science.1228604
8. Correa-Baena J-P, Saliba M, Buonassisi T et al (2017) Science 358:739. https://doi.org/10.1126/science.aam6323
9. Ball JM, Lee MM, Hey A et al (2013) Energy Environ Sci 6:1739. https://doi.org/10.1039/C3EE40810H
10. Yang WS, Noh JH, Jeon NJ et al (2015) Science 348:1234. https://doi.org/10.1126/science.aaa9272
11. Yang WS, Park B-W, Jung EH et al (2017) Science 356:1376. https://doi.org/10.1126/science.aan2301
12. Liang Z, Zhang Y, Xu H et al (2023). Nature. https://doi.org/10.1038/s41586-023-06784-0
13. Mariotti S, Köhnen E, Scheler F et al (2023) Science 381:63. https://doi.org/10.1126/science.adf5872
14. Khenkin MV, Katz EA, Abate A et al (2020) Nat Energy 5:35. https://doi.org/10.1038/s41560-019-0529-5
15. Katz EA (2020) Nat Energy 5:1. https://doi.org/10.1038/s41560-020-0552-6
16. D'Innocenzo V, Srimath Kandada AR, De Bastiani M et al (2014) J Am Chem Soc 136:17730. https://doi.org/10.1021/ja511198f

17. Deschler F, Price M, Pathak S et al (2014) J Phys Chem Lett 5:1421. https://doi.org/10.1021/jz5005285

18. Tan Z-K, Moghaddam RS, Lai ML et al (2014) Nat Nanotechnol 9:687. https://doi.org/10.1038/nnano.2014.149

19. Stranks SD, Snaith HJ (2015) Nat Nanotechnol 10:391. https://doi.org/10.1038/nnano.2015.90

20. Yin W-J, Shi T, Yan Y (2014) Appl Phys Lett 104:063903. https://doi.org/10.1063/1.4864778

21. de Quilettes DW, Vorpahl SM, Stranks SD et al (2015) Science 348:683. https://doi.org/10.1126/science.aaa5333

22. Droseros N, Longo G, Brauer JC et al (2018) ACS Energy Lett 3:1458. https://doi.org/10.1021/acsenergylett.8b00475

23. Schmidt LC, Pertegás A, González-Carrero S et al (2014) J Am Chem Soc 136:850. https://doi.org/10.1021/ja4109209

24. Manser JS, Christians JA, Kamat PV (2016) Chem Rev 116:12956. https://doi.org/10.1021/acs.chemrev.6b00136

25. Travis W, Glover ENK, Bronstein H et al (2016) Chem Sci 7:4548. https://doi.org/10.1039/C5SC04845A

26. Whitfield PS, Herron N, Guise WE et al (2016) Sci Rep 6:35685. https://doi.org/10.1038/srep35685

27. Thomson S (2018) Application Note: Edinburgh Instruments.

28. Lee J-H, Bristowe NC, Lee JH et al (2016) Chem Mater 28:4259. https://doi.org/10.1021/acs.chemmater.6b00968

29. Kurlansky M, Schindler S (2006) The story of salt. G.P. Putnam's Sons

30. Kasai H, Nalwa HS, Oikawa H et al (1992) Jpn J Appl Phys 31:L1132. https://doi.org/10.1143/jjap.31.l1132

31. Zhao YS, Fu H, Peng A et al (2008) Adv Mater 20:2859. https://doi.org/10.1002/adma.200800604

32. Papavassiliou GC, Pagona G, Karousis N et al (2012) J Mater Chem 22:8271. https://doi.org/10.1039/C2JM15783G

33. Zhang F, Zhong H, Chen C et al (2015) ACS Nano 9:4533. https://doi.org/10.1021/acsnano.5b01154

34. Xing J, Yan F, Zhao Y et al (2016) ACS Nano 10:6623. https://doi.org/10.1021/acsnano.6b01540

35. Levchuk I, Osvet A, Tang X et al (2017) Nano Lett 17:2765. https://doi.org/10.1021/acs.nanolett.6b04781

36. Li X, Wu Y, Zhang S et al (2016) Adv Funct Mater 26:2435. https://doi.org/10.1002/adfm.201600109

37. Leng M, Chen Z, Yang Y et al (2016) Angew Chem Int Ed 55:15012. https://doi.org/10.1002/anie.201608160

38. Yang B, Chen J, Hong F et al (2017) Angew Chem Int Ed 56:12471. https://doi.org/10.1002/anie.201704739

39. Leng M, Yang Y, Zeng K et al (2018) Adv Funct Mater 28:1704446. https://doi.org/10.1002/adfm.201704446

40. Zhang J, Yang Y, Deng H et al (2017) ACS Nano 11:9294. https://doi.org/10.1021/acsnano.7b04683

41. Zhang F, Huang S, Wang P et al (2017) Chem Mater 29:3793. https://doi.org/10.1021/acs.chemmater.7b01100

42. Murray CB, Norris DJ, Bawendi MG (1993) J Am Chem Soc 115:8706. https://doi.org/10.1021/ja00072a025

43. Chang J, Waclawik ER (2014) RSC Adv 4:23505. https://doi.org/10.1039/C4RA02684E

44. Protesescu L, Yakunin S, Bodnarchuk MI et al (2015) Nano Lett 15:3692. https://doi.org/10.1021/nl5048779

45. Akkerman QA, Park S, Radicchi E et al (2017) Nano Lett 17:1924. https://doi.org/10.1021/acs.nanolett.6b05262

46. Han C, Li C, Zang Z et al (2017) Photon Res 5:473. https://doi.org/10.1364/PRJ.5.000473

47. Protesescu L, Yakunin S, Bodnarchuk MI et al (2016) J Am Chem Soc 138:14202. https://doi.org/10.1021/jacs.6b08900

48. Lignos I, Protesescu L, Emiroglu DB et al (2018) Nano Lett 18:1246. https://doi.org/10.1021/acs.nanolett.7b04838

49. Protesescu L, Yakunin S, Kumar S et al (2017) ACS Nano 11:3119. https://doi.org/10.1021/acsnano.7b00116

50. Vybornyi O, Yakunin S, Kovalenko MV (2016) Nanoscale 8:6278. https://doi.org/10.1039/C5NR06890H

51. Imran M, Caligiuri V, Wang M et al (2018) J Am Chem Soc 140:2656. https://doi.org/10.1021/jacs.7b13477

52. Roy M, Vikram, Banerjee S et al (2019) Chem Eur J 25:9892. https://doi.org/10.1002/chem.201805859

53. Liu F, Zhang Y, Ding C et al (2017) ACS Nano 11:10373. https://doi.org/10.1021/acsnano.7b05442

54. Wu L, Zhong Q, Yang D et al (2017) Langmuir 33:12689. https://doi.org/10.1021/acs.langmuir.7b02963

55. Liu P, Chen W, Wang W et al (2017) Chem Mater 29:5168. https://doi.org/10.1021/acs.chemmater.7b00692

56. Chen M, Zou Y, Wu L et al (2017) Adv Func Mater 27:1701121. https://doi.org/10.1002/adfm.201701121

57. Parveen S, Paul KK, Giri PK (2020) ACS Appl Mater Interfaces 12:6283. https://doi.org/10.1021/acsami.9b20896

58. Pan Q, Hu H, Zou Y et al (2017) J Mater Chem C 5:10947. https://doi.org/10.1039/C7TC03774K

59. Shamsi J, Rastogi P, Caligiuri V et al (2017) ACS Nano 11:10206. https://doi.org/10.1021/acsnano.7b04761

60. Liu H, Wu Z, Gao H et al (2017) ACS Appl Mater Interfaces 9:42919. https://doi.org/10.1021/acsami.7b14677

61. Jang DM, Kim DH, Park K et al (2016) J Mater Chem C 4:10625. https://doi.org/10.1039/C6TC04213A

62. Tong Y, Bladt E, Aygüler MF et al (2016) Angew Chem Int Ed 55:13887. https://doi.org/10.1002/anie.201605909

63. Roy M, Vikram, Bhawna et al (2021) J Phys Chem Lett 12:1189. https://doi.org/10.1021/acs.jpclett.0c03426

64. Leupold N, Schötz K, Cacovich S et al (2019) ACS Appl Mater Interfaces 11:30259. https://doi.org/10.1021/acsami.9b09160

65. Dou B, Wheeler LM, Christians JA et al (2018) ACS Energy Lett 3:979. https://doi.org/10.1021/acsenergylett.8b00305

66. Hintermayr VA, Richter AF, Ehrat F et al (2016) Adv Mater 28:9478. https://doi.org/10.1002/adma.201602897

67. Zhu Z-Y, Yang Q-Q, Gao L-F et al (2017) J Phys Chem Lett 8:1610. https://doi.org/10.1021/acs.jpclett.7b00431

68. Baláž P, Achimovičová M, Baláž M et al (2013) Chem Soc Rev 42:7571. https://doi.org/10.1039/C3CS35468G

69. Protesescu L, Yakunin S, Nazarenko O et al (2018) ACS Appl Nano Mater 1:1300. https://doi.org/10.1021/acsanm.8b00038

70. Chen D, Li J, Chen X et al (2019) ACS Appl Mater Interfaces 11:10059. https://doi.org/10.1021/acsami.8b19002

71. Sichert JA, Tong Y, Mutz N et al (2015) Nano Lett 15:6521. https://doi.org/10.1021/acs.nanolett.5b02985

72. Sandeep K, Padmakumar K, Ambili KU et al (2022). Physica Status Solidi B-Basic Solid State Phys. https://doi.org/10.1002/pssb.202100600

73. Byranvand MM, Otero-Martinez C, Ye JZ et al (2022). Adv Opt Mater. https://doi.org/10.1002/adom.202200423

74. Jiang H, Cui S, Chen Y et al (2021) Nano Select 2:2040. https://doi.org/10.1002/nano.202100084

75. Swarnkar A, Mir WJ, Nag A (2018) ACS Energy Lett 3:286. https://doi.org/10.1021/acsenergylett.7b01197

76. Qiu Z, Li N, Huang Z et al (2020) Small Methods 4:1900877. https://doi.org/10.1002/smtd.201900877

77. Ogomi Y, Morita A, Tsukamoto S et al (2014) J Phys Chem Lett 5:1004. https://doi.org/10.1021/jz5002117

78. Hao F, Stoumpos CC, Chang RPH et al (2014) J Am Chem Soc 136:8094. https://doi.org/10.1021/ja5033259

79. Hao F, Stoumpos CC, Cao DH et al (2014) Nat Photonics 8:489. https://doi.org/10.1038/nphoton.2014.82

80. Liu C, Fan J, Li H et al (2016) Sci Rep 6:35705. https://doi.org/10.1038/srep35705
81. Zhang X, Cao W, Wang W et al (2016) Nano Energy 30:511. https://doi.org/10.1016/j.nanoen.2016.10.039
82. Deng J, Wang H, Xun J et al (2020) Mater Des 185:108246. https://doi.org/10.1016/j.matdes.2019.108246
83. Jellicoe TC, Richter JM, Glass HFJ et al (2016) J Am Chem Soc 138:2941. https://doi.org/10.1021/jacs.5b13470
84. Babayigit A, Duy Thanh D, Ethirajan A et al (2016) Sci Rep 6:18721. https://doi.org/10.1038/srep18721
85. Parobek D, Roman BJ, Dong Y et al (2016) Nano Lett 16:7376. https://doi.org/10.1021/acs.nanolett.6b02772
86. Liu W, Lin Q, Li H et al (2016) J Am Chem Soc 138:14954. https://doi.org/10.1021/jacs.6b08085
87. Mir WJ, Jagadeeswararao M, Das S et al (2017) ACS Energy Lett 2:537. https://doi.org/10.1021/acsenergylett.6b00741
88. van der Stam W, Geuchies JJ, Altantzis T et al (2017) J Am Chem Soc 139:4087. https://doi.org/10.1021/jacs.6b13079
89. Shen X, Zhang Y, Kershaw SV et al (2019) Nano Lett 19:1552. https://doi.org/10.1021/acs.nanolett.8b04339
90. Bi C, Wang S, Li Q et al (2019) J Phys Chem Lett 10:943. https://doi.org/10.1021/acs.jpclett.9b00290
91. De A, Das S, Mondal N et al (2019) ACS Mater Lett 1:116. https://doi.org/10.1021/acsmaterialslett.9b00101
92. Thawarkar S, Rana PJS, Narayan R et al (2019) Langmuir 35:17150. https://doi.org/10.1021/acs.langmuir.9b02450
93. Yong Z-J, Guo S-Q, Ma J-P et al (2018) J Am Chem Soc 140:9942. https://doi.org/10.1021/jacs.8b04763
94. Zhou Y, Yong Z-J, Zhang K-C et al (2016) J Phys Chem Lett 7:2735. https://doi.org/10.1021/acs.jpclett.6b01147
95. Abdelhady AL, Saidaminov MI, Murali B et al (2016) J Phys Chem Lett 7:295. https://doi.org/10.1021/acs.jpclett.5b02681
96. Nayak PK, Sendner M, Wenger B et al (2018) J Am Chem Soc 140:574. https://doi.org/10.1021/jacs.7b11125
97. Lozhkina OA, Murashkina AA, Shilovskikh VV et al (2018) J Phys Chem Lett 9:5408. https://doi.org/10.1021/acs.jpclett.8b02178
98. Begum R, Parida MR, Abdelhady AL et al (2017) J Am Chem Soc 139:731. https://doi.org/10.1021/jacs.6b09575
99. Zhang X, Wang H, Hu Y et al (2019) J Phys Chem Lett 10:1750. https://doi.org/10.1021/acs.jpclett.9b00790
100. Liu M, Zhong G, Yin Y et al (2017) Adv Sci 4:1700335. https://doi.org/10.1002/advs.201700335
101. Balakrishnan SK, Kamat PV (2018) Chem Mater 30:74. https://doi.org/10.1021/acs.chemmater.7b04142
102. Palazon F, Almeida G, Akkerman QA et al (2017) Chem Mater 29:4167. https://doi.org/10.1021/acs.chemmater.7b00895
103. Udayabhaskararao T, Houben L, Cohen H et al (2018) Chem Mater 30:84. https://doi.org/10.1021/acs.chemmater.7b02425
104. Liu Z, Bekenstein Y, Ye X et al (2017) J Am Chem Soc 139:5309. https://doi.org/10.1021/jacs.7b01409
105. Palazon F, Urso C, De Trizio L et al (2017) ACS Energy Lett 2:2445. https://doi.org/10.1021/acsenergylett.7b00842
106. Palazon F, Dogan S, Marras S et al (2017) J Phys Chem C 121:11956. https://doi.org/10.1021/acs.jpcc.7b03389
107. Turedi B, Lee KJ, Dursun I et al (2018) J Phys Chem C 122:14128. https://doi.org/10.1021/acs.jpcc.8b01343
108. Xiao G, Cao Y, Qi G et al (2017) J Am Chem Soc 139:10087. https://doi.org/10.1021/jacs.7b05260
109. Huisman BAH, Palazon F, Bolink HJ (2021). Inorg Chem. https://doi.org/10.1021/acs.inorgchem.1c00212
110. Cordero SR, Carson PJ, Estabrook RA et al (2000) J Phys Chem B 104:12137. https://doi.org/10.1021/jp001771s

111. Motti SG, Patel JB, Oliver RDJ et al (2021) Nat Commun 12:6955. https://doi.org/10.1038/s41467-021-26930-4

112. Yuan H, Debroye E, Janssen K et al (2016) J Phys Chem Lett 7:561. https://doi.org/10.1021/acs.jpclett.5b02828

113. Hoke ET, Slotcavage DJ, Dohner ER et al (2015) Chem Sci 6:613. https://doi.org/10.1039/C4SC03141E

114. Wang Y, Li X, Sreejith S et al (2016) Adv Mater 28:10637. https://doi.org/10.1002/adma.201604110

115. Ha SK, Mauck CM, Tisdale WA (2019) Chem Mater 31:2486. https://doi.org/10.1021/acs.chemmater.8b05310

116. Roy M, Vikram, Bhawna et al (2021) Phys Chem Chem Phys 23:27355. https://doi.org/10.1039/D1CP03529K

117. Sen A, Chatterjee S, Sen P (2022) J Phys Chem C 126:18057. https://doi.org/10.1021/acs.jpcc.2c05987

118. Bekenstein Y, Koscher BA, Eaton SW et al (2015) J Am Chem Soc 137:16008. https://doi.org/10.1021/jacs.5b11199

119. Zhang D, Eaton SW, Yu Y et al (2015) J Am Chem Soc 137:9230. https://doi.org/10.1021/jacs.5b05404

120. Almeida G, Goldoni L, Akkerman Q et al (2018) ACS Nano 12:1704. https://doi.org/10.1021/acsnano.7b08357

121. Pan A, He B, Fan X et al (2016) ACS Nano 10:7943. https://doi.org/10.1021/acsnano.6b03863

122. Tyagi P, Arveson SM, Tisdale WA (2015) J Phys Chem Lett 6:1911. https://doi.org/10.1021/acs.jpclett.5b00664

123. Akkerman QA, Motti SG, Srimath Kandada AR et al (2016) J Am Chem Soc 138:1010. https://doi.org/10.1021/jacs.5b12124

124. Bertolotti F, Nedelcu G, Vivani A et al (2019) ACS Nano 13:14294. https://doi.org/10.1021/acsnano.9b07626

125. Shamsi J, Kubicki D, Anaya M et al (2020) ACS Energy Lett 5:1900. https://doi.org/10.1021/acsenergylett.0c00935

126. Weidman MC, Seitz M, Stranks SD et al (2016) ACS Nano 10:7830. https://doi.org/10.1021/acsnano.6b03496

127. Shamsi J, Dang Z, Bianchini P et al (2016) J Am Chem Soc 138:7240. https://doi.org/10.1021/jacs.6b03166

128. Weidman MC, Goodman AJ, Tisdale WA (2017) Chem Mater 29:5019. https://doi.org/10.1021/acs.chemmater.7b01384

129. Saidaminov MI, Mohammed OF, Bakr OM (2017) ACS Energy Lett 2:889. https://doi.org/10.1021/acsenergylett.6b00705

130. Koutselas IB, Ducasse L, Papavassiliou GC (1996) J Phys: Condens Matter 8:1217. https://doi.org/10.1088/0953-8984/8/9/012

131. Ishihara T, Takahashi J, Goto T (1989) Solid State Commun 69:933. https://doi.org/10.1016/0038-1098(89)90935-6

132. Tong Y, Bohn BJ, Bladt E et al (2017) Angew Chem Int Ed 56:13887. https://doi.org/10.1002/anie.201707224

133. Zhang D, Yu Y, Bekenstein Y et al (2016) J Am Chem Soc 138:13155. https://doi.org/10.1021/jacs.6b08373

134. Fang H-H, Adjokatse S, Wei H et al (2016) Sci Adv 2:e1600534. https://doi.org/10.1126/sciadv.1600534

135. Gordillo G, Otálora CA, Reinoso MA (2017) J Appl Phys 122:075304. https://doi.org/10.1063/1.4999297

136. Agiorgousis ML, Sun Y-Y, Zeng H et al (2014) J Am Chem Soc 136:14570. https://doi.org/10.1021/ja5079305

137. Kim Y-H, Wolf C, Kim Y-T et al (2017) ACS Nano 11:6586. https://doi.org/10.1021/acsnano.6b07617

138. Queisser HJ, Haller EE (1998) Science 281:945. https://doi.org/10.1126/science.281.5379.945

139. Freysoldt C, Grabowski B, Hickel T et al (2014) Rev Mod Phys 86:253. https://doi.org/10.1103/RevModPhys.86.253

140. Kim J, Lee S-H, Lee JH et al (2014) J Phys Chem Lett 5:1312. https://doi.org/10.1021/jz500370k

141. Eames C, Frost JM, Barnes PRF et al (2015) Nat Commun 6:7497. https://doi.org/10.1038/ncomms8497
142. Buin A, Pietsch P, Xu J et al (2014) Nano Lett 14:6281. https://doi.org/10.1021/nl502612m
143. Xu J, Buin A, Ip AH et al (2015) Nat Commun 6:7081. https://doi.org/10.1038/ncomms8081
144. Buin A, Comin R, Xu J et al (2015) Chem Mater 27:4405. https://doi.org/10.1021/acs.chemmater.5b01909
145. Ball JM, Petrozza A (2016) Nat Energy 1:16149. https://doi.org/10.1038/nenergy.2016.149
146. Walsh A, Scanlon DO, Chen S et al (2015) Angew Chem Int Ed 54:1791. https://doi.org/10.1002/anie.201409740
147. Wang Y-N, Ma P, Peng L-M et al (2017) Acta Phys Chim Sin 33:2099. https://doi.org/10.3866/PKU.WHXB201705115
148. Leng M, Yang Y, Chen Z et al (2018) Nano Lett 18:6076. https://doi.org/10.1021/acs.nanolett.8b03090
149. Dutta A, Behera RK, Dutta SK et al (2018) J Phys Chem Lett 9:6599. https://doi.org/10.1021/acs.jpclett.8b02825
150. Das Adhikari S, Behera RK, Bera S et al (2019) J Phys Chem Lett 10:1530. https://doi.org/10.1021/acs.jpclett.9b00599
151. Woo JY, Kim Y, Bae J et al (2017) Chem Mater 29:7088. https://doi.org/10.1021/acs.chemmater.7b02669
152. Mondal N, De A, Samanta A (2019) ACS Energy Lett 4:32. https://doi.org/10.1021/acsenergylett.8b01909
153. Li C, Chen X, Li N et al (2020) J Mater Chem C 8:3694. https://doi.org/10.1039/C9TC06854F
154. Mosconi E, Merabet B, Meggiolaro D et al (2018) J Phys Chem C 122:14107. https://doi.org/10.1021/acs.jpcc.8b01307
155. Lu C-H, Biesold-McGee GV, Liu Y et al (2020) Chem Soc Rev 49:4953. https://doi.org/10.1039/C9CS00790C
156. Ono LK, Juarez-Perez EJ, Qi Y (2017) ACS Appl Mater Interfaces 9:30197. https://doi.org/10.1021/acsami.7b06001
157. Zhou H, Chen Q, Li G et al (2014) Science 345:542. https://doi.org/10.1126/science.1254050
158. Ling L, Yuan S, Wang P et al (2016) Adv Funct Mater 26:5028. https://doi.org/10.1002/adfm.201601557
159. Leguy AMA, Hu Y, Campoy-Quiles M et al (2015) Chem Mater 27:3397. https://doi.org/10.1021/acs.chemmater.5b00660
160. Ahn N, Kwak K, Jang MS et al (2016) Nat Commun 7:13422. https://doi.org/10.1038/ncomms13422
161. Aristidou N, Eames C, Sanchez-Molina I et al (2017) Nat Commun 8:15218. https://doi.org/10.1038/ncomms15218
162. Brenes R, Eames C, Bulović V et al (2018) Adv Mater 30:1706208. https://doi.org/10.1002/adma.201706208
163. Huang H, Chen B, Wang Z et al (2016) Chem Sci 7:5699. https://doi.org/10.1039/C6SC01758D
164. Mukherjee A, Roy M, Pathoor N et al (2021) J Phys Chem C 125:17133. https://doi.org/10.1021/acs.jpcc.1c02207
165. Stoeckel M-A, Gobbi M, Bonacchi S et al (2017) Adv Mater 29:1702469. https://doi.org/10.1002/adma.201702469
166. Merdasa A, Bag M, Tian Y et al (2016) J Phys Chem C 120:10711. https://doi.org/10.1021/acs.jpcc.6b03512
167. Yuan G, Ritchie C, Ritter M et al (2018) J Phys Chem C 122:13407. https://doi.org/10.1021/acs.jpcc.7b11168
168. Yang J-H, Yin W-J, Park J-S et al (2016) J Mater Chem A 4:13105. https://doi.org/10.1039/C6TA03599J
169. Kim H-S, Jang I-H, Ahn N et al (2015) J Phys Chem Lett 6:4633. https://doi.org/10.1021/acs.jpclett.5b02273
170. Li C, Tscheuschner S, Paulus F et al (2016) Adv Mater 28:2446. https://doi.org/10.1002/adma.201503832
171. Yoon SJ, Kuno M, Kamat PV (2017) ACS Energy Lett 2:1507. https://doi.org/10.1021/acsenergylett.7b00357
172. Hentz O, Zhao Z, Gradečak S (2016) Nano Lett 16:1485. https://doi.org/10.1021/acs.nanolett.5b05181

173. Yoon SJ, Draguta S, Manser JS et al (2016) ACS Energy Lett 1:290. https://doi.org/10.1021/acsenergylett.6b00158
174. Bischak CG, Hetherington CL, Wu H et al (2017) Nano Lett 17:1028. https://doi.org/10.1021/acs.nanolett.6b04453
175. Barker AJ, Sadhanala A, Deschler F et al (2017) ACS Energy Lett 2:1416. https://doi.org/10.1021/acsenergylett.7b00282
176. Mosconi E, De Angelis F (2016) ACS Energy Lett 1:182. https://doi.org/10.1021/acsenergylett.6b00108
177. Zhang H, Fu X, Tang Y et al (2019) Nat Commun 10:1088. https://doi.org/10.1038/s41467-019-09047-7
178. Unger EL, Kegelmann L, Suchan K et al (2017) J Mater Chem A 5:11401. https://doi.org/10.1039/C7TA00404D
179. Ravi VK, Markad GB, Nag A (2016) ACS Energy Lett 1:665. https://doi.org/10.1021/acsenergylett.6b00337
180. Samu GF, Scheidt RA, Kamat PV et al (2018) Chem Mater 30:561. https://doi.org/10.1021/acs.chemmater.7b04321
181. Lee C, Kim K, Shin Y et al (2021). Front Energy Res. https://doi.org/10.3389/fenrg.2020.605976
182. Mulder JT, du Fossé I, Alimoradi Jazi M et al (2021) ACS Energy Lett 6:2519. https://doi.org/10.1021/acsenergylett.1c00970
183. Wong JM, Xu J, Zhang R et al (2021) J Phys Chem C 125:13696. https://doi.org/10.1021/acs.jpcc.1c04335
184. Tang L, Wei J, Cai Z et al (2021) Electrochem Commun 131:107123. https://doi.org/10.1016/j.elecom.2021.107123